Modelling the Fracture Behavior of a 350WT Steel

Rick Link
Brian Yuen
Lei Jiang
Martec Limited

Prepared By:
Martec Limited
400-1800 Brunswick Street
Halifax, Nova Scotia B3J 3J8 Canada

Contractor's Document Number: TR-14-56 (Reference Number: 13.40156)
Contract Project Manager: David Whitehouse, 902-425-5101
PWGSC Contract Number: W7707-145705
CSA: Christopher Bayley, Group Leader, Corrosion and Metallurgy, 250-363-4784

Contract Report
DRDC-RDDC-2014-C175
May 2014

Lloyd's Register Marine

Working together for a safer world

Modelling the Fracture Behavior of a 350WT Steel

Martec Technical Report # TR-14-56
Martec Reference Number: 13.40156

May 2014

Prepared for:

Christopher Bayley
DRDC Atlantic Dockyard Laboratory Pacific
CFB Esquimalt, Building 199
PO Box 17000, Station Forces
Victoria, British Columbia
Canada
V9A-7N2

Martec Limited
1888 Brunswick Street, Suite 400
Halifax, Nova Scotia B3J 3J8 Canada

tel. 902.425.5101
fax. 902.421.1923
email. martec-info@lr.org
www.martec.com

REVISION CONTROL

REVISION	REVISION DATE
1.0	March 24, 2014
2.0	April 29, 2014

SIGNATURE PAGE

MODELLING THE FRACTURE BEHAVIOR OF A 350WT STEEL

Technical Report # TR-14-56 Rev 02
Martec Reference Number: 13.40156
12 May 2014

Prepared by: _____ **Date:** May 12/14
Rick Link
Senior Research Engineer

Prepared by: _____ **Date:** May 12/14
Brian Yuen
Research Engineer

Reviewed by: _____ **Date:** May 12, 2014
Lei Jiang
Senior Research Engineer

Approved by: _____ **Date:** May 12, 2014
David Whitehouse
Manager, Research and Product Development

EXECUTIVE SUMMARY

This report is a summary of work performed to apply fracture tools developed in previous studies to a number of different tests on 350WT steel. This work is a continuation of two previous studies: the first involved the development and implementation of a micromechanical failure model, and the second developed a finite element post-processor to compute strain energy release rates and Weibull stresses.

The project was divided into a number of phases. The first phase was to determine temperature and strain rate dependent material properties from published sources. Ductile and brittle fracture parameters for the Gurson failure criteria were then determined through FE calibration with existing Charpy V-notch (CVN) and dynamic tear ductile-to-brittle transition (DBT) data. Once the parameters were obtained, the model was applied to DBT analyses of a CVN parametric study involving specimen width, and an explosive loading test.

The CVN parametric study indicated that there was an increase in top shelf energy with increasing width, which is consistent with expected results. However, there was little or no change in the transition temperature with increasing specimen width, which was not expected. Analysis of the explosive loading test indicated that ductile, brittle and mixed fracture modes were present at varying temperatures, and that the explosive transition temperature was between 0° and 10° C.

There were significant differences between the fracture parameters obtained for the CVN and dynamic tear tests; these should be unique values for any test. Possible methods of resolution include increased mesh densities, fitting more ductile parameters, and inclusion of nonlocal effects for both brittle and ductile parameters.

TABLE OF CONTENTS

LIST OF FIGURES

LIST OF TABLES

1.0 INTRODUCTION

Steels exhibit a competitive failure mechanism that is dependent upon both temperature and strain rate. At elevated temperatures and relatively low strain rates, the failure mechanism is dominated by plastic void nucleation, growth, and eventual void coalescence, while at lower temperatures and higher strain rates, a cleavage fracture mechanism dominates. The competition between these micro-mechanisms determines the macroscopic fracture resistance, and is quantified empirically through the ductile to brittle (DBT) transition curves.

As part of W7707-9-8254 and W7707-13-5632, a constitutive failure model was implemented as a user-defined model subroutine within the finite element code LS-DYNA. The model was calibrated with, and validated against experimental Dynamic Tear data, with the numerical results reproducing the experimental ductile-to-brittle transition. However, as the cleavage fracture process is known to be specimen size and loading geometry dependent, the predicted ductile-to-brittle transition temperature is limited to the calibrated configurations.

The current requirements are to extend the application of the user-defined material model to study the size and geometry dependence of fracture, to compare the calculated fracture energy with elastic-plastic fracture mechanics, and to conduct a parametric study to identify the most sensitive values to fracture.

The tasks for completion are as follows:

Task 1: Material Property Characterization

1) Develop and implement a rational procedure to include the flow stress dependence associated with low temperatures.
2) Compute the strain energy release rate, *J*, with statically loaded compact tension tests, and compare with experimental values.
3) Compute the Beremin material parameters from the available notched tensile test data.

Task 2: Dynamic Modelling

1) Obtain a rational estimate of the variation of flow stress with strain rate.
2) Use the available Charpy V-notch (CVN) and dynamic tear tests to obtain the necessary ductile fracture (Gurson) and critical cleavage fracture stress.

Task 3: Modelling the Size Dependence of Fracture

1) Using the obtained material parameters from Tasks 1 and 2, perform a DBT parametric study on CVN specimens varying in thickness from 0.5B to 1.5B.
2) Perform a DBT FE analysis of the explosive loading test detailed in [13].

Task 4: Final Report

The final report is organized as follows. Section 2 describes the determination of material properties, including flow stress as a function of temperature and strain rate. Section 3 describes the computation of J for the compact tension specimens, and Section 4 details the determination of the brittle and ductile material parameters from the CVN and dynamic tear tests. Section 5 shows the setup and results of both the CVN parametric study and the explosive loading test. Finally, Section 6 summarizes the report results, and recommends future areas of study.

2.0 MATERIAL PROPERTIES

This section describes the determination of fundamental material properties, including the flow stress as a function of temperature, mechanical strain, and strain rate. These properties are then verified through analysis of a series of notched tests performed by the SA [1].

2.1 THERMAL DEPENDENCE OF FLOW STRESS

It is well known that there is a significant increase in flow stress for decreasing temperatures. Figure 2.1 shows a plot of Bouchard's [2] data for G40.21-50 steel. The average strength increase between initial yield and ultimate was used for the plot, and the data was curve fit to the expression

$$\sigma_y = \sigma_{y296}\left(\frac{T}{296}\right)^{-0.3761} \qquad [2.1]$$

where σ_{y296} is the yield strength at 296° K, and T is the temperature in degrees Kelvin.

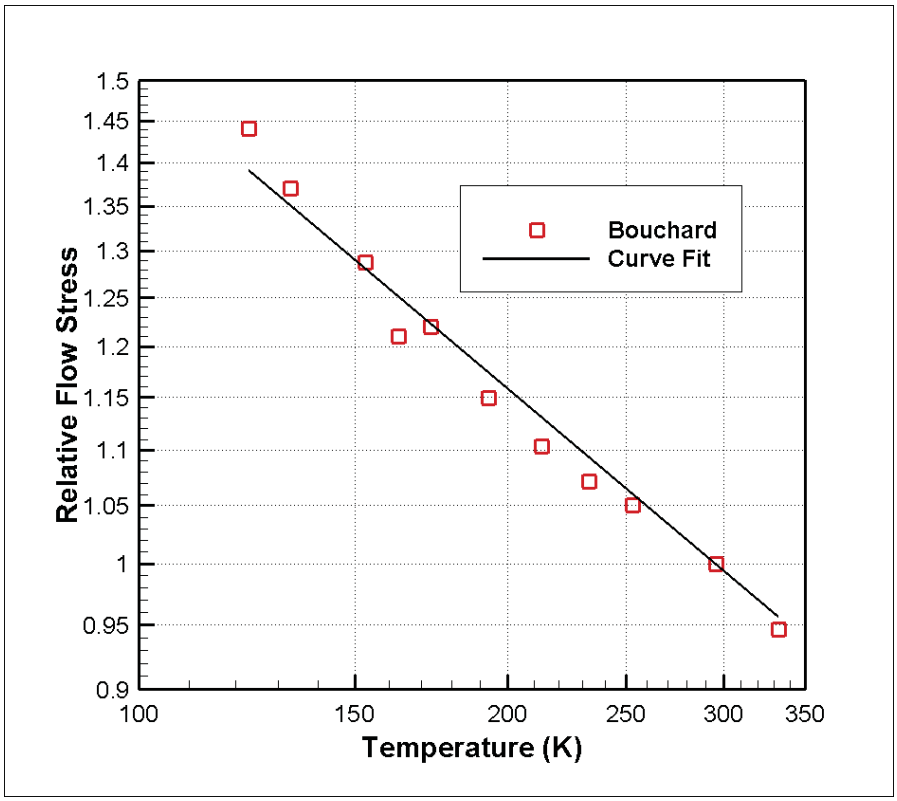

Figure 2.1: Flow Stress vs. Temperature (Data From [2])

2.2 MECHANICAL STRAIN DEPENDENCE AND NOTCHED TESTS

The mechanical strain dependence expression from [3] is used here

$$\sigma_y = 344.0 + 500.0\left(\varepsilon^p\right)^{0.3} \qquad [2.2]$$

where ε^p is the effective plastic strain.

A series of notched specimens were tested by the SA, and the data was initially provided in order to determine critical cleavage fracture stresses using the Beremin methodology [4]. The specimens were prepared according to ESIS P6-98 [5], except that flat rather than round specimens were used. The determination of the critical cleavage fracture stress assumes a brittle failure mode; after investigation of the data, it was determined that the failure mode was ductile for all tests, and hence not suitable for Beremin analysis. However, the tests can be used as verification of the static properties of 350WT steel.

Three specimen notch geometries were tested; 2, 4 and 10 mm radii. Figure 2.2 shows the specimen dimensions, with a thickness of 9 mm. Figure 2.3 shows the FE mesh geometries; one-half symmetry with 18 through-thickness elements was used. The full grip end was not modelled; the grip end was restrained from transverse translation in order to simulate friction grips. The material model *MAT_PIECEWISE_MULTILINEAR was used in the analyses in order to use an implicit time integration scheme to reduce solution runtimes. Currently, an implicit material model is not available for the JCG user-defined model.

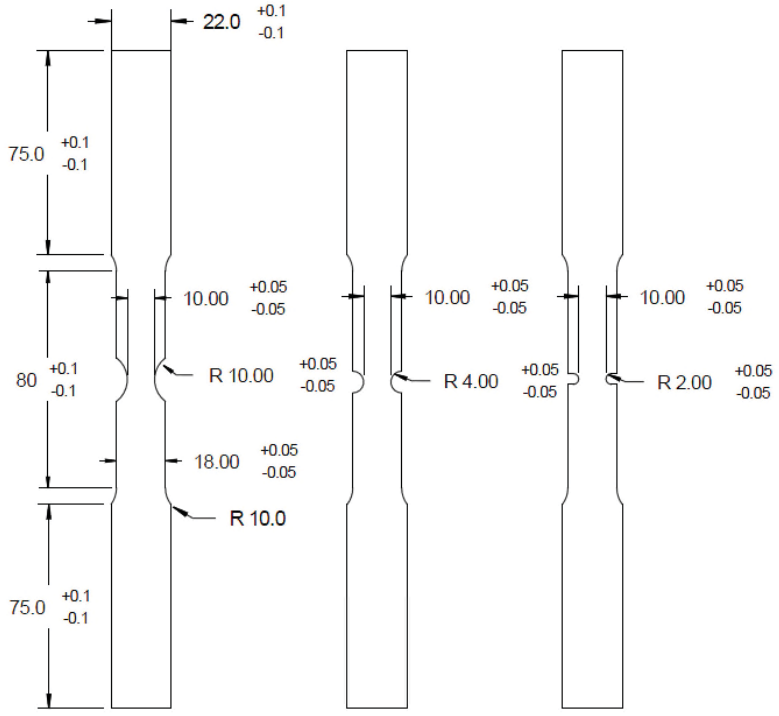

Figure 2.2: Notched Test Specimen Dimensions

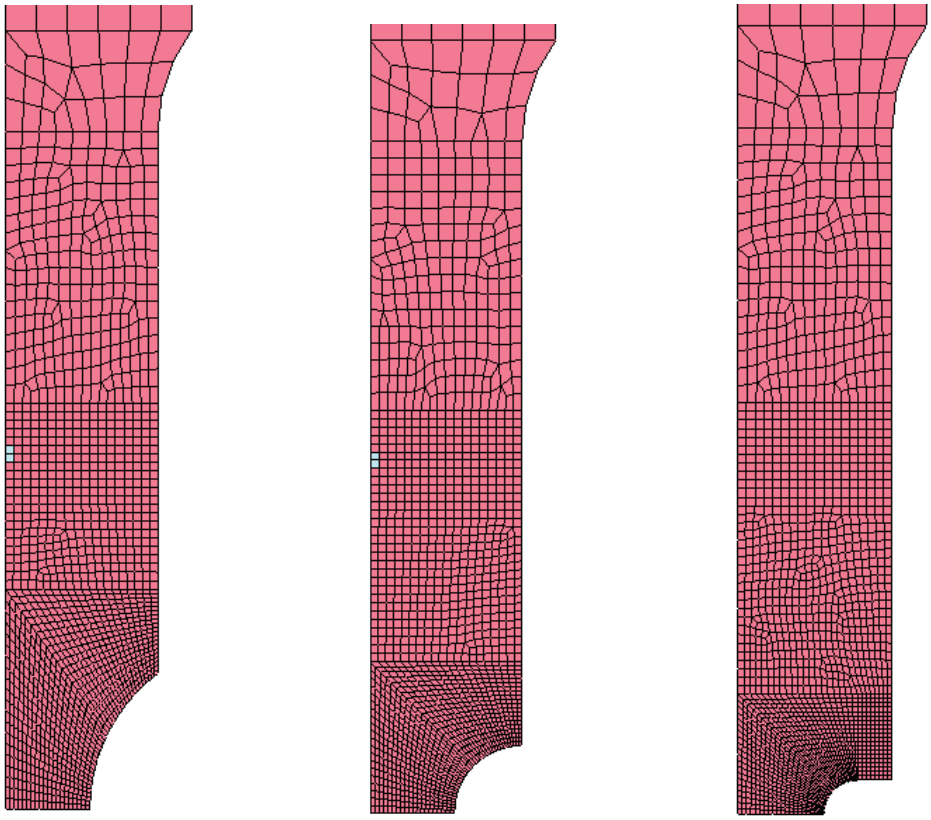

Figure 2.3: Notched Specimen Meshes – 10, 4, 2 mm (L to R)

The specimens were all tested at 123° K, so Equation 2.1 was used to adjust Equation 2.2 to account for low temperature. Displacement control was used in order to obtain load post-peak response. Comparisons are made to peak load attained, and the cross-sectional failure area. Since failure is not predicted in the FE models, the analysis cross-sectional areas are compared at identical ratios of failure to peak load. For example, if the analysis peak load is 80 kN, and the experimental peak and failure loads are 75 and 55 kN, respectively, the FE cross-sectional area at (55/75)x80 = 58.66 kN is compared.

Table 2.1: Notched Test Results Comparison

Notch Size (mm)	Peak Load (kN)	Failure Load (kN)	Failure Width (mm)	Failure Thickness (mm)	Failure Area (mm^2)
10 mm Exp	73.86	50.96	7.08	5.60	39.65
10 mm FE	75.94	52.40	6.43	5.28	33.95
4 mm Exp	79.36	53.79	7.65	5.45	41.69
4 mm FE	80.45	54.53	6.37	4.80	30.58
2 mm Exp	80.19	56.28	7.91	5.52	43.66
2 mm FE	83.35	58.50	6.56	4.86	31.88

Comparison of results shown in Table 2.1 shows that peak loads match well, with a maximum difference of 4%. However, there is a distinct trend when failure areas are compared. The FE failure areas are consistently less than the experimental results, on average around 25%. This may be due to neglecting void nucleation and coalescence, as found in the Gurson model, which would tend to increase the necked area.

Figure 2.4 shows a view looking into the notch of a 2 mm specimen (Specimen R09-02) at failure. It can be seen that there is pronounced necking in both the FE and experimental views. The experimental failure seems to have initiated by a through-thickness crack, followed by tearing at the crack tip. Subsequent metallurgical testing revealed a layer of pearlite due to the plate rolling process that may have been the through-thickness crack initiator [3].

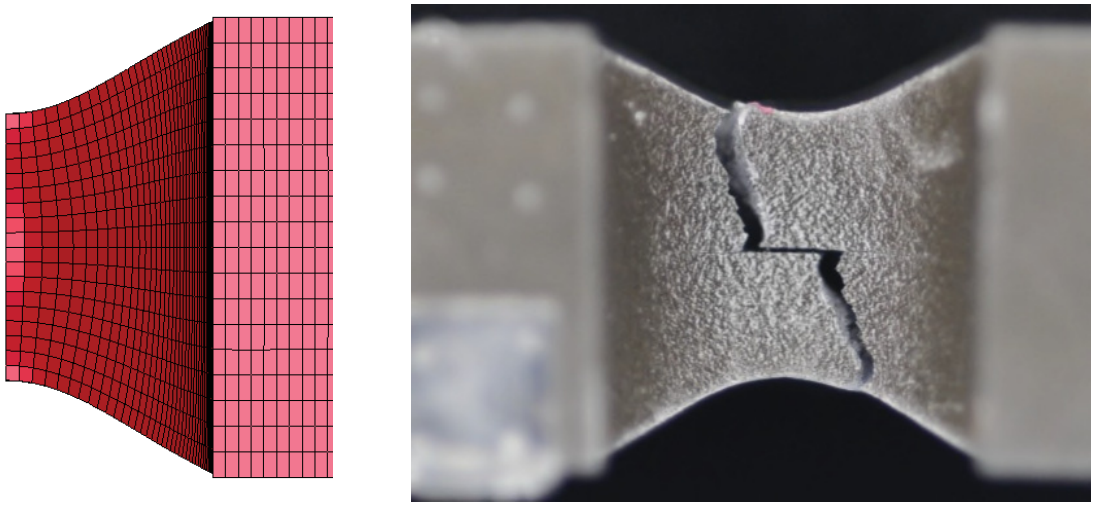

Figure 2.4: Cross-Section Comparison at Failure

Most experimental failures occurred away from the notch center; a typical failure site is shown for Specimen 06-R02 in Figure 2.5. Investigation of the FE results was unable to determine why the failures occurred in these unexpected regions. The pearlite layer may have caused this anomalous behavior by forming a crack initiation site away from the central notch region.

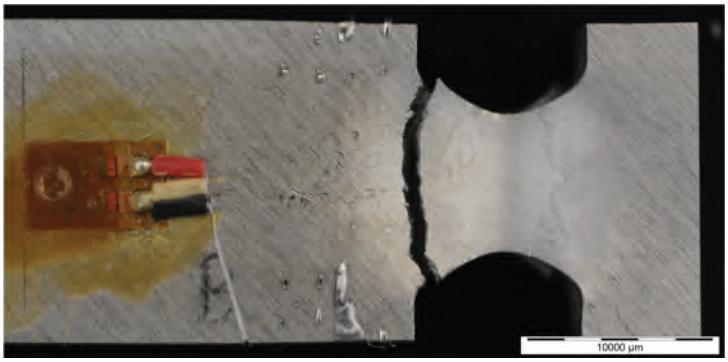

Figure 2.5: Typical Failure Site

2.3 STRAIN RATE DEPENDENCE

The expression

$$\sigma_y = \left[344.0 + 500.0\left(\varepsilon^p\right)^{0.3}\right]\left[1 + 0.02\ln\left(\frac{\dot{\varepsilon}}{3\times10^{-4}}\right)\right]\left(\frac{T}{296}\right)^{-0.3761} \qquad [2.3]$$

is used to incorporate the effects of mechanical strain, temperature, and strain rate on the flow stress, where $\dot{\varepsilon}$ is a measure of the strain rate. In a previous study [1], the strain rate expression incorporated a value of C = 0.035. However, this assumed that the Gurson constants were fixed for all analyses, which is not the case in this study. A curve fit value of C = 0.02 is adopted here, which is consistent with data provided for 350 HSLA steel [7]. This steel has flow stress characteristics consistent with 350WT, and is a large dataset.

3.0 J-INTEGRAL CALCULATIONS

In this section, the J-integral calculation routines developed in [8] are used to compute *J* for three tested compact tension specimens. Initially, an LS-DYNA analysis is performed using Equation 2.3 (without strain rate effects and ductile failure) in conjunction with the *MAT_PIECEWISE_MULTILINEAR plasticity model in order to determine stresses, strains, and deformation gradients. The data is then read and *J* is computed for various loading levels. The *J* values obtained from the 3 experimental failure loads are then compared with FE *J* values.

3.1 COMPACT TENSION TEST SETUP

Figure 3.1 shows the specimen dimensions, and Figure 3.2 shows the FE mesh used in the analysis. The 3 specimens tested are in conformance with the ASTM E-1820-11 standard.

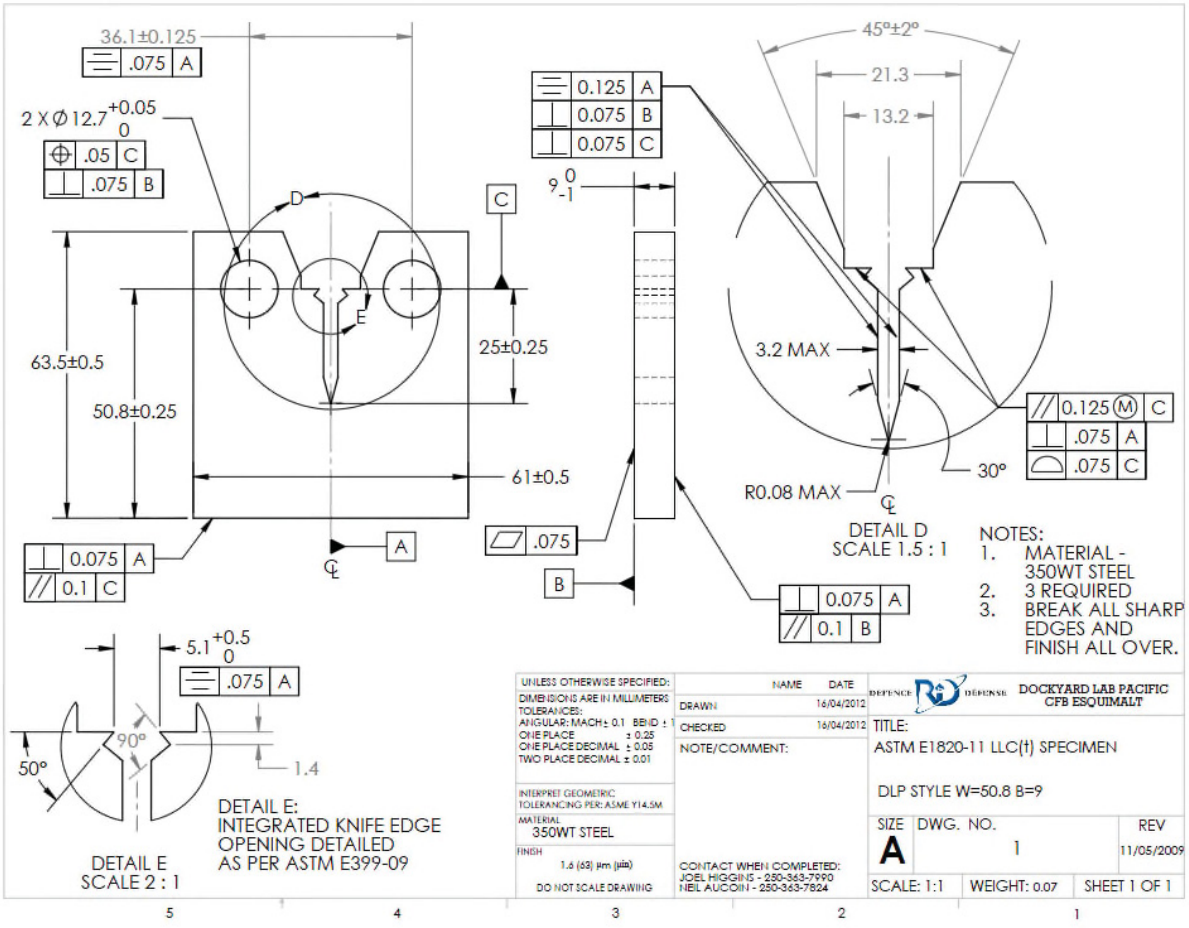

Figure 3.1: Compact Tension Specimen Dimensions

The FE meshes do not include the detail near the crack opening (Detail E in Figure 3.1); it was felt that this was not necessary to obtain accurate results. The mesh is arranged in a regular fashion near the crack tip in order to use the J-integral contour generator.

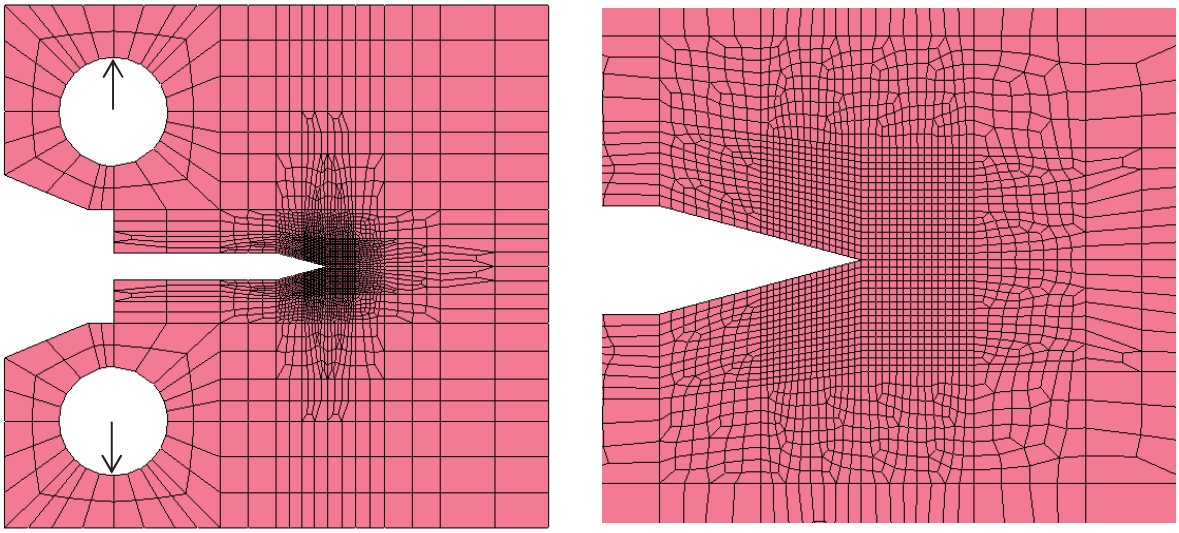

Figure 3.2: Compact Tension FE Mesh

Once the FE analysis was conducted, the J-integrals were computed for the nearest 15 contours to the crack tip. Figure 3.3 shows *J* as a function of failure load; as the number of contours is increased, the values appear to converge to unique values. It is apparent that the first few contours produce somewhat lower *J* values; this is to be expected, since *J* calculations should be performed over the entire plastic zone. This is not the case for the first few contours.

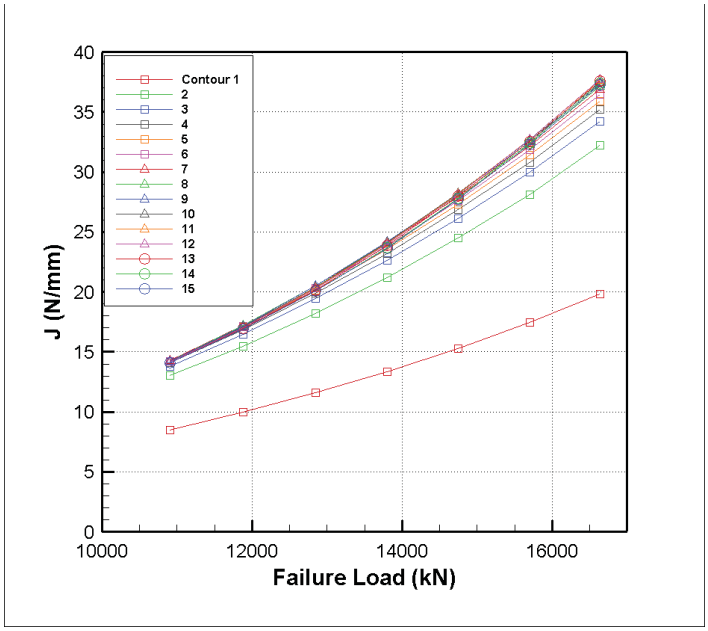

Figure 3.3: J Calculated For All Contours

Figure 3.4 compares the FE results for the 12th contour to the 3 experiments. Two comparisons are made: experimental *J* computed with and without the precrack included. This is done because the effect of precracking was not included in the FE analysis. It is apparent that the FE results are nearly bounded by experiment

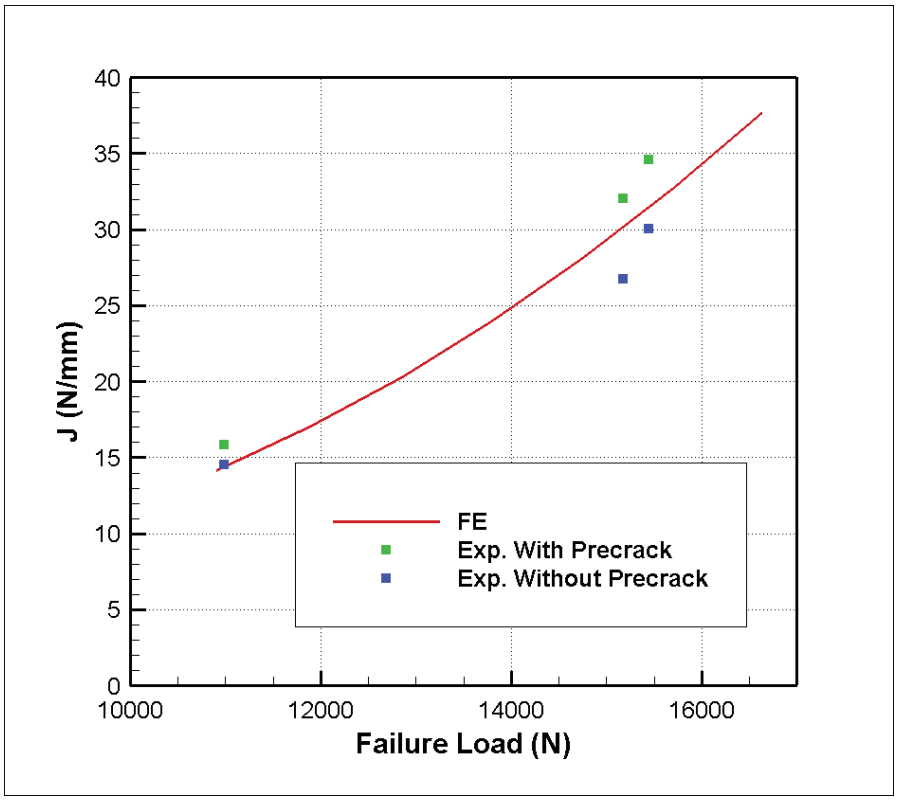

Figure 3.4: Computed J – FE vs. Experimental Results

4.0 DETERMINATION OF FRACTURE PARAMETERS

In order to model dynamic fracture tests such as drop tower or Charpy V-notch, both flow stress, yield surface evolution, and cleavage fracture must be properly characterized. Suitable flow stress parameters have been determined in Section 2. It remains to obtain Gurson and cleavage fracture parameters that produce numerical results consistent with experimental data. The Scientific Authority has provided experimental DBT data for Charpy V-notch and drop tower tests for calibration of the fracture material parameters.

Ductile fracture is controlled by void nucleation and coalescence, which are built into the Gurson micromechanical model. The equations governing the yield surface evolution are [1]

$$F = \frac{1}{2} s_{ij} s_{ij} - \frac{1}{3} \sigma_y \left(1 - 2 q_1 f^* \cosh\left(-\frac{1}{2} q_2 \frac{\sigma_{kk}}{\sigma_y} \right) + \left(q_1 f^* \right)^2 \right) = 0 \qquad [4.1]$$

$$f^* = \begin{cases} f & f \le f_C \\ f_C + \left(\left(1/q_1 - f_C \right) / \left(f_F - f_C \right) \right) \left(f - f_C \right) & f \ge f_C \end{cases} \qquad [4.2]$$

$$df = \left(1 - f \right) d\varepsilon_{kk}^P + A \, d\varepsilon^P \qquad [4.3]$$

$$A = \frac{f_N}{s_N \sqrt{2\pi}} \exp\left(-\frac{1}{2} \left(\frac{\varepsilon^P - \varepsilon_N}{s_N} \right)^2 \right) \qquad [4.4]$$

From the above equations, the Gurson material parameters are q_1, q_2, f_C, f_F, f_N, s_N, and ε_N. This is a formidable set of parameters to fit to experimental data. As well, to include nonlocal effects, the fit parameters should be as a function of element length. In LS-DYNA's Gurson model [14], f_C, f_F, f_N and the initial void fraction, f_0 , can be described as functions of element length. The volume fraction of void nucleating particles, f_N, is chosen in this study. Brittle fracture is dominated by cleavage fracture, which is currently controlled using the critical cleavage fracture stress, σ_{cr}. Since fracture is a material softening process and is mesh dependent, values of σ_{cr} and f_N apply to individual mesh sizes.

The procedure for obtaining σ_{cr} and f_N for a given mesh size is as follows:

1) The top shelf energy of the DBT curve is used to determine f_N. f_N is varied in the FE analysis until the correct top shelf energy is obtained. σ_{cr} is fixed at a large value, which implies full ductile failure, and the flow stress is assumed to be at room temperature values.

2) The energy at the transition point (50% top shelf energy) is used to determine σ_{cr}. The temperature at this energy is obtained from experiment, and the flow stress parameters are adjusted using Equation 2.3. Using f_N values obtained from Step 1, σ_{cr} is varied until the transition point energy is obtained (or close).
3) The DBT curve is run to determine goodness of fit.

Table 4.1 shows the fixed Gurson parameters used. In this study, it was decided to remove void coalescence as a variable, and set f_C and f_F approximately equal i.e. only void nucleation is considered here.

Table 4.1: Fixed Gurson Parameters

Gurson Parameter	Value
q_1	1.2
q_2	1.0
f_c	0.245
f_f	0.250
s_N	0.10
ε_N	0.30

4.1 CHARPY V-NOTCH TESTS

4.1.1 Test Setup

The notched bar impact testing was performed in accordance to ASTM E23-96 [9]. In the tests performed by DRDC Atlantic, Charpy V-notch (CVN) specimens were impact loaded in three-point bending with a pendulum machine, and the total energy loss during separation is recorded. During the test, the CVN specimen sits in front of the anvil and is fractured by the striker tup of the pendulum that is released from an initial height and strikes the specimen horizontally, as shown in Figure 4.1. In the DRDC Atlantic tests, the mass of the pendulum was 30.239 kg while the initial height of the drop was 1.372 m. The dimensions of the CVN specimen and the striker tup used in the DRDC Atlantic tests are shown in Figure 4.2 and Figure 4.3, respectively. The Charpy fracture energy (E_{CVN}) is then calculated as the difference between the initial potential energy (PE_i) and the final energy (PE_f) of the pendulum after it fracture the specimen, as given by the following equation:

$$E_{CVN} = PE_i - PE_f = \frac{1}{2}mv_i^2 - \frac{1}{2}mv_f^2 \qquad [4.5]$$

where, m is the mass of the pendulum (30.239 kg), v_i is the velocity of the pendulum just before contacting the specimen (5.18 m/s) and v_f is the velocity of the pendulum after fracturing the specimen.

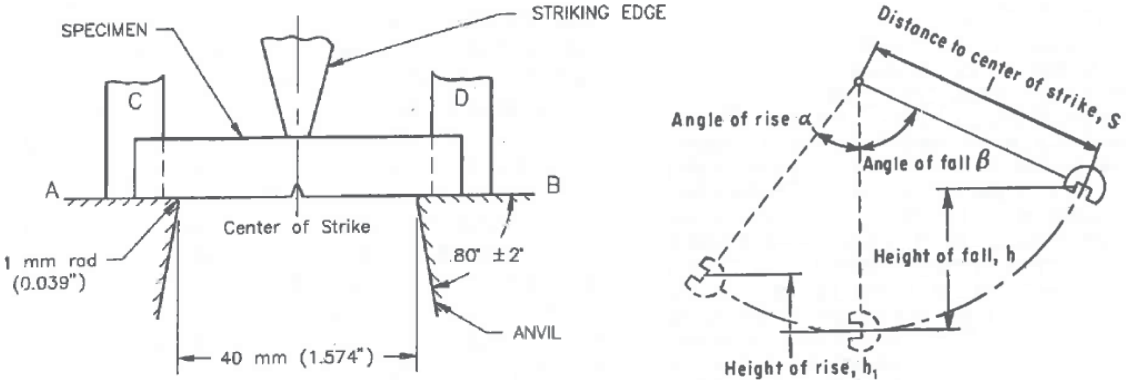

Figure 4.1: Charpy V-Notch Specimen, Anvil Supports and Striker [9]

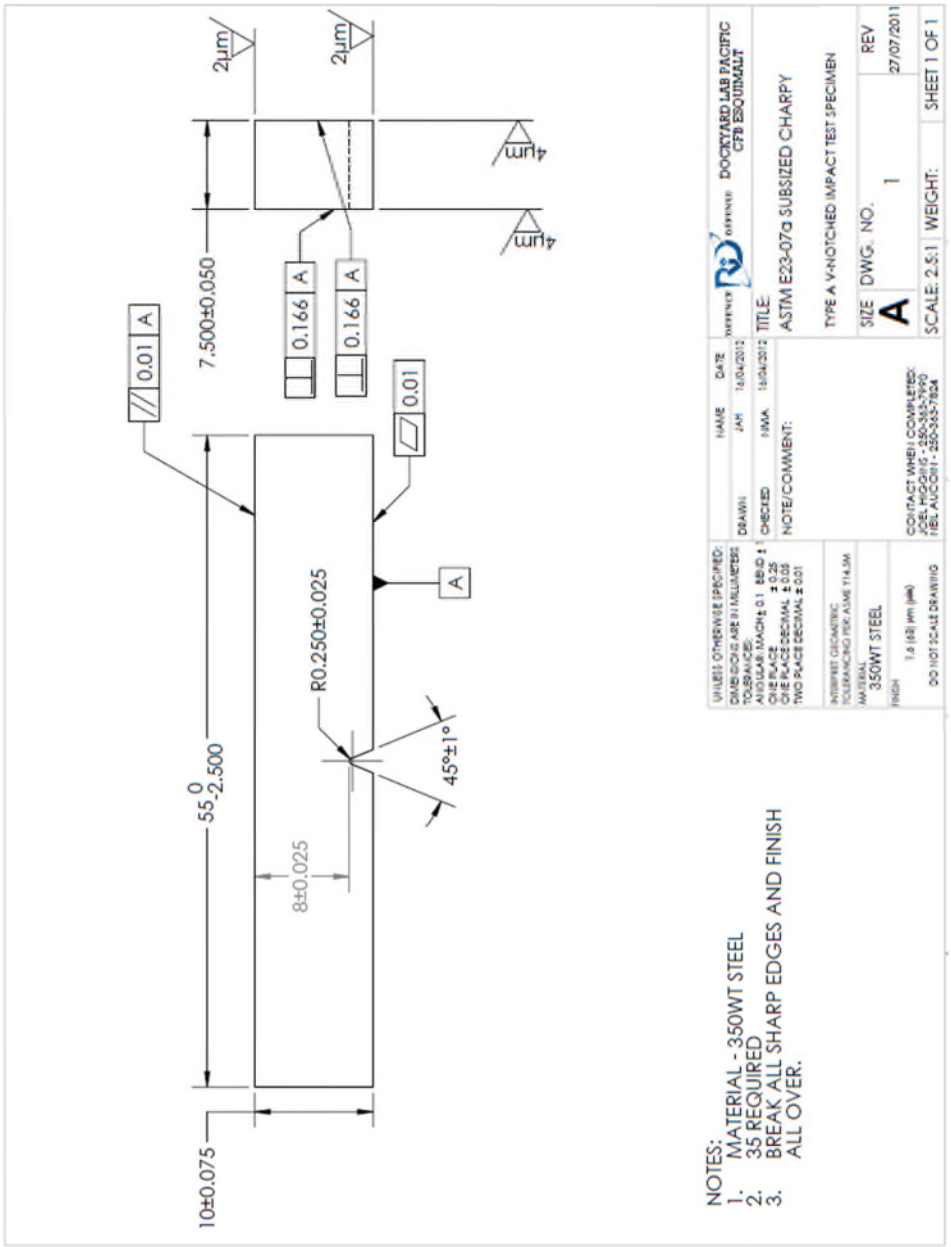

Figure 4.2: Dimensions of the Charpy V-Notch Specimen

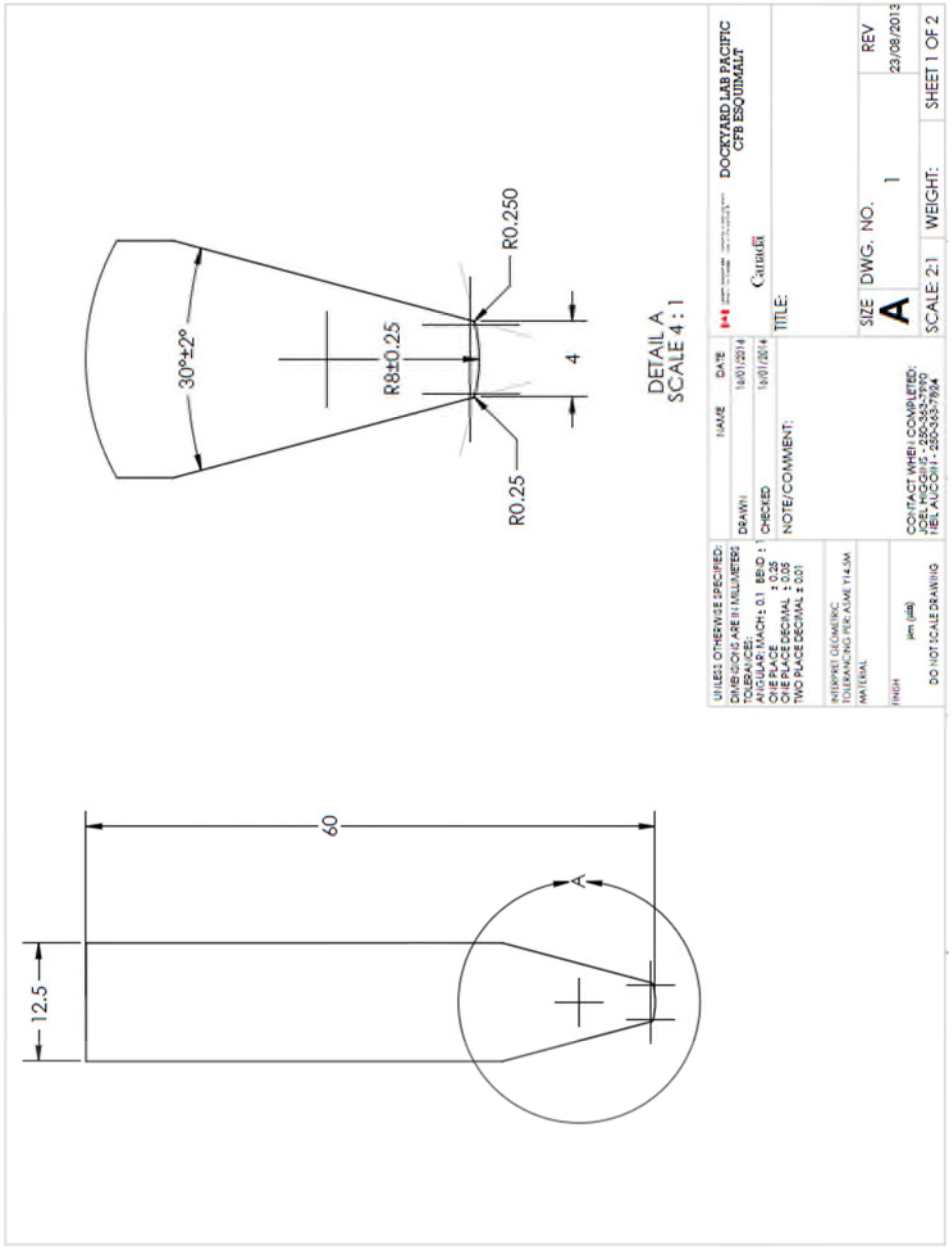

Figure 4.3: Dimensions of the Striker Tup for the Notched Bar Impact Testing

4.1.2 Analysis Setup and Results

Figures 4.4 and 4.5 show a side and overhead view, respectively, of the FE mesh used in the analyses. A quarter symmetry model was initially selected; this resulted in several non-physical crack propagation patterns that significantly affected results. For this reason, a half symmetry model is used. The center mesh resolution is 0.25 mm, and is graded out from the notch tip. To simulate the saw-cut at the symmetry axis, the two adjacent element sets are pre-weakened by imposing a small initial void fraction there. Rollers are placed at the boundaries to simulate the knife edges. An initial velocity of 5.188 m/s is imposed on the tup, and contact surfaces are used between the specimen top and the tup.

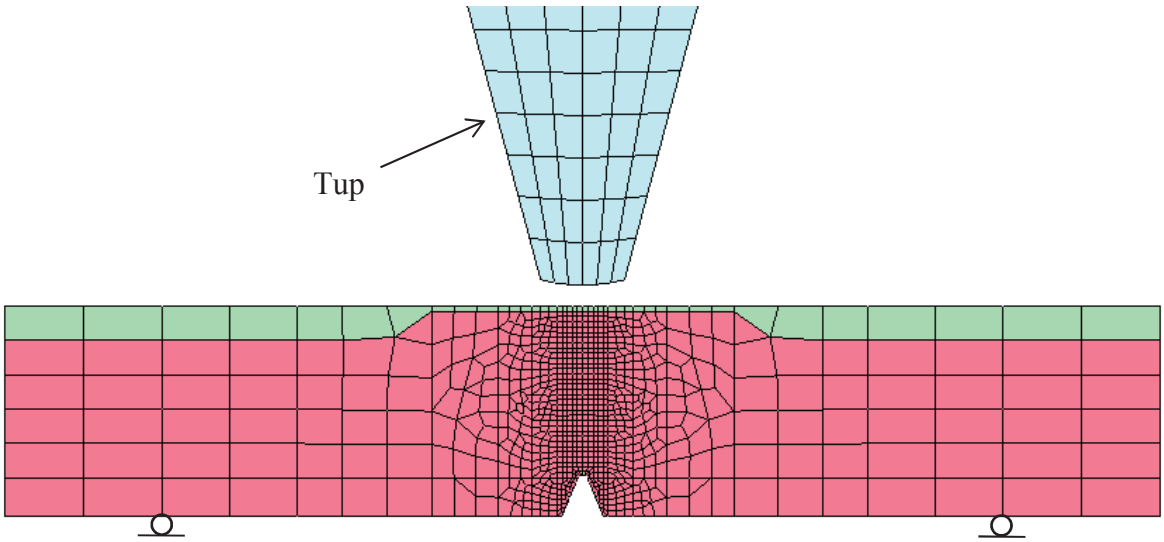

Figure 4.4: Charpy V-Notch FE Mesh – Side View

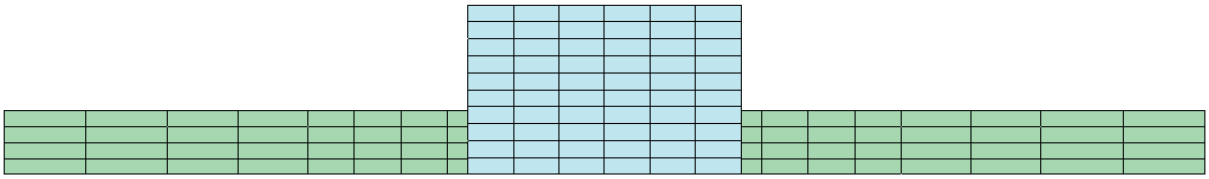

Figure 4.5: Charpy V-Notch FE Mesh – Top View

Values of σ_{cr} and f_N were determined as 1950 MPa and 0.010, respectively. Figure 4.6 shows the DBT curve. Although the transition appears to be more abrupt, the analysis results are a good match to experiment.

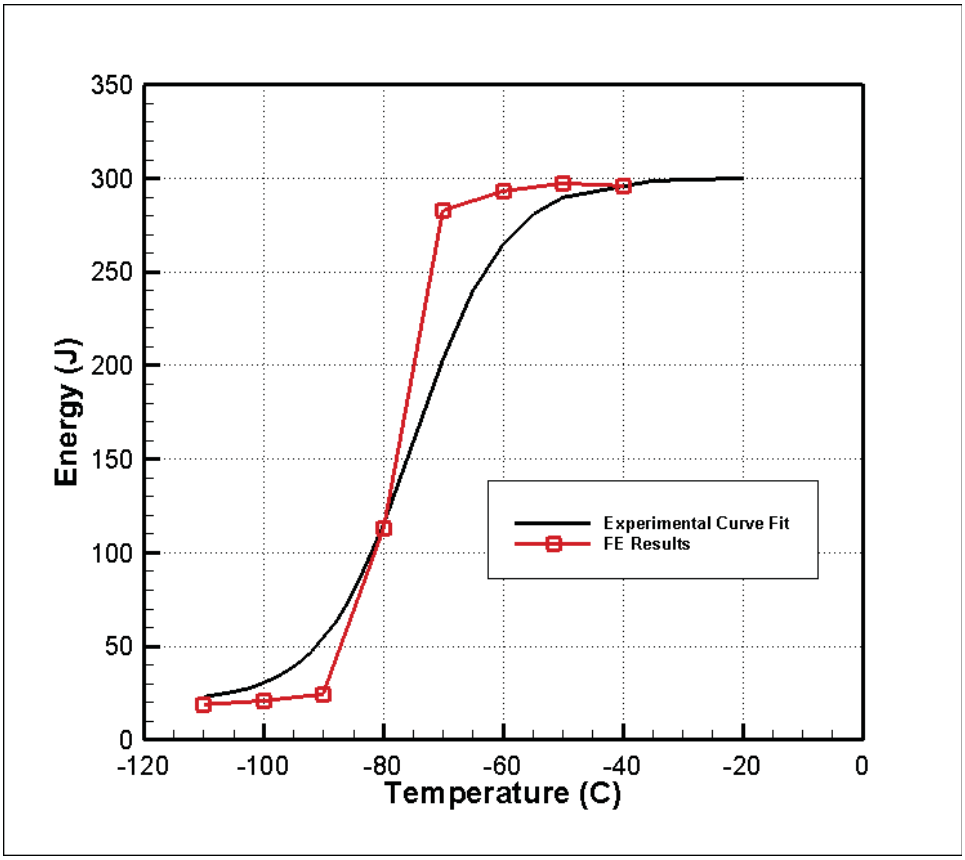

Figure 4.6: Charpy Test – FE vs. Experiment

For ductile failures, the specimen fails due to void formation up to about 40-50% of the cross-section, followed by brittle failure above that. Figures 4.7-4.9 illustrate the failure progression at -40° C. Figure 4.7 shows the specimen just before first breakage at the notch; the notch is significantly blunted at this point. The specimen then undergoes extreme deformations and strains, as evidenced by Figure 4.8, which is just before the onset of brittle failure. Finally, the specimen crack stresses exceed σ_{cr} and fractures in a brittle manner suddenly.

Figure 4.10 and 4.11 show the mesh just before and after brittle fracture onset, respectively. The void fraction is fringe plotted, with a failure fraction of 0.25. It can be seen that the mesh is severely deformed in the crack propagation area before brittle fracture. After brittle fracture has occurred, 12-15 elements fail in a relatively short time period.

The actual test at -40° C did not fail all the way through the specimen. It is suspected that the extremely large deformations caused the specimen to fall through the apparatus before complete fracture had occurred.

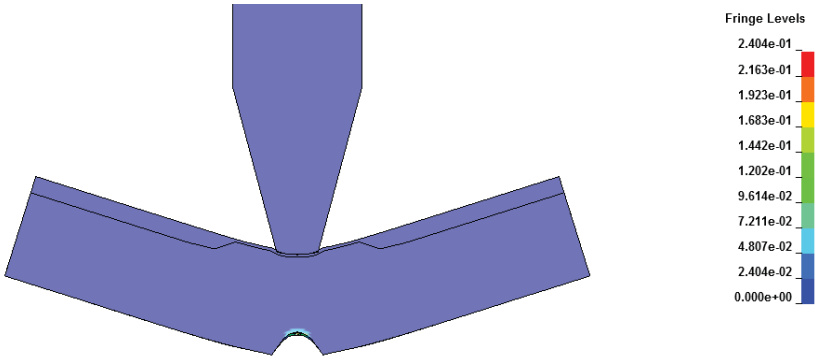

Figure 4.7: Charpy – Initial Notch Failure - -40° C (Fringe units are dimensionless)

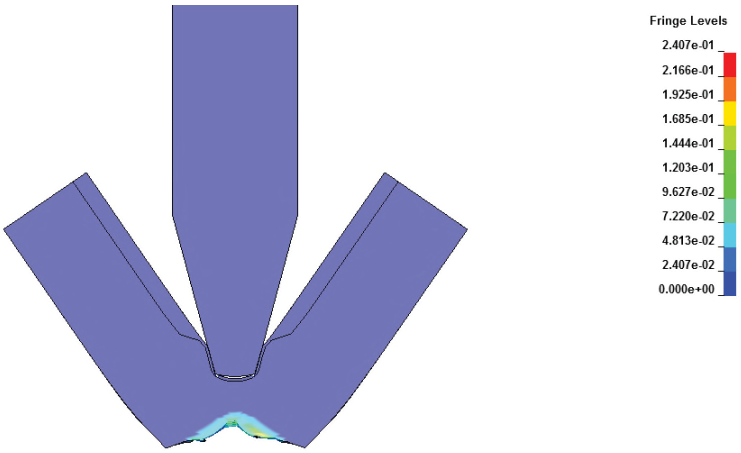

Figure 4.8: Charpy – Before Brittle Failure - -40° C

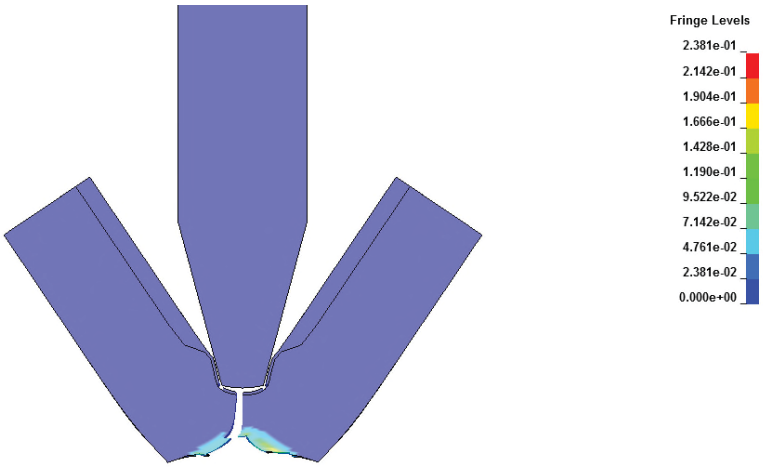

Figure 4.9: Charpy – After Brittle Failure - -40° C

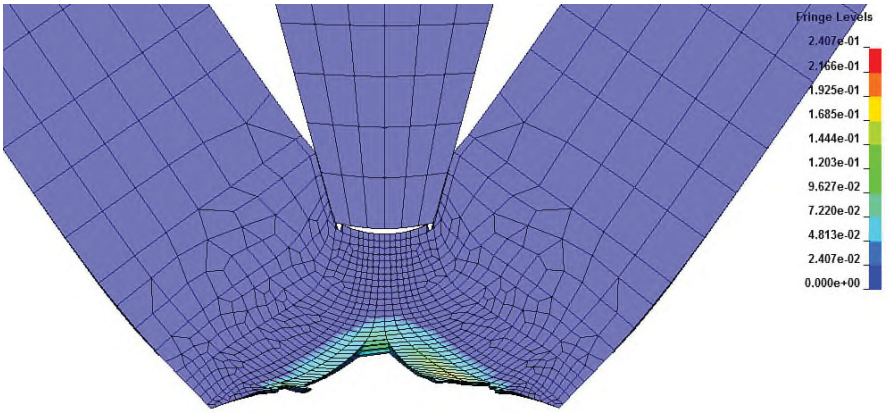

Figure 4.10: Charpy FE Mesh Before Fracture - -40° C

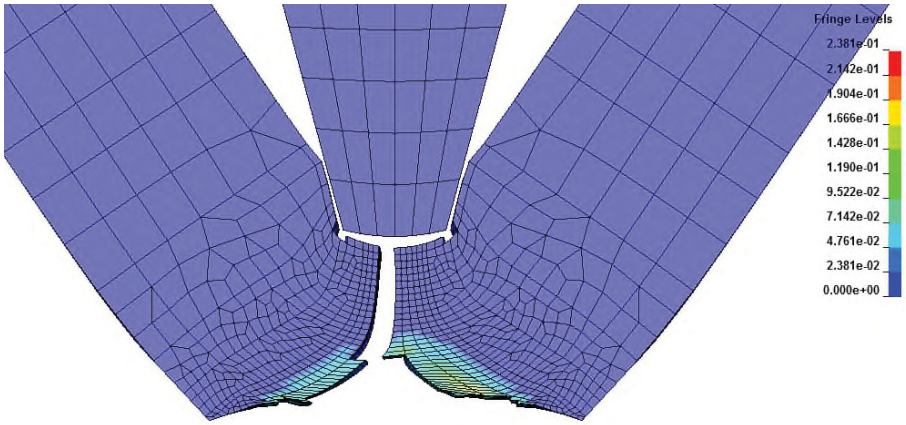

Figure 4.11: Charpy FE Mesh After Fracture - -40° C

Figure 4.12 shows the fracture surface area after failure for both the FE analysis and experiment at the transition temperature (-80° C). The FE result exhibits a significant necked region in approximately the same location as the tested specimen. In addition, a brittle fracture region occurred in the test specimen from approximately the specimen center to the top, as evidenced by roughness in that central region. This also approximately matches the brittle region in the FE analysis. However, the periphery of the test specimen in the brittle fracture area contains a shear lip that is not reproduced in the analysis. This is probably due to a lack of refinement in the FE mesh in this area. However, the FE results show good agreement with the experimentally observed absorbed energy and failure surface.

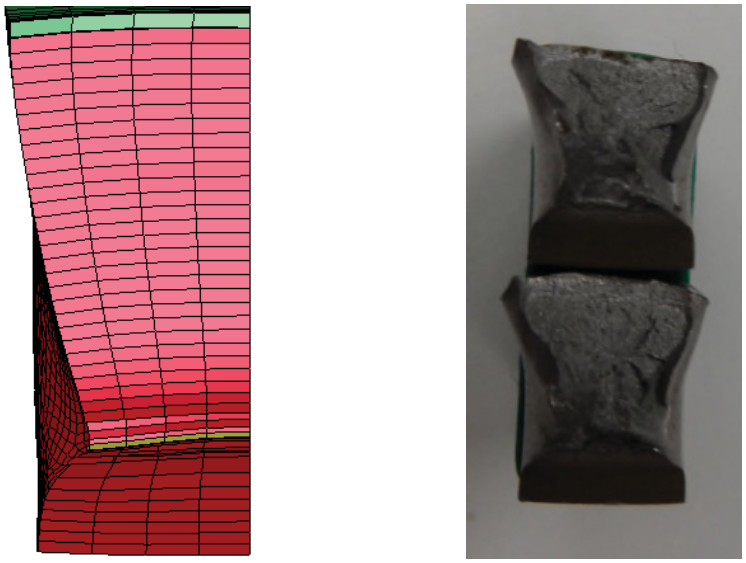

Figure 4.12: Charpy Fracture Surface - -80° C

Figure 4.13 shows the FE fracture surface at the transition temperature of -80° C. Initially, ductile failure occurred near the crack tip (2-3 elements), followed by a brittle failure that rapidly propagated through the specimen.

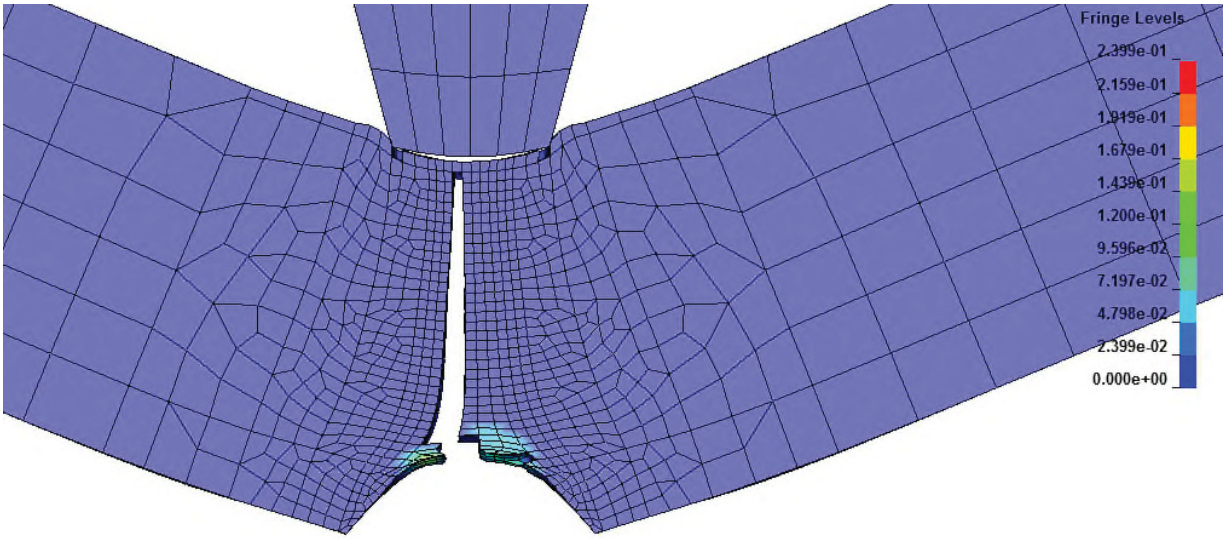

Figure 4.13: Charpy – Failure - -80° C

4.2 DYNAMIC TEAR TESTS

4.2.1 Test Setup

The dynamic tear testing was performed in accordance to ASTM E604 [10]. The test involves a single-edge notched beam (DT specimen) that is impact loaded in three-point bending, and the total energy loss during separation is recorded. In the tests performed by DRDC Atlantic, the DT specimens were fractured with a drop-weight machine. A typical drop-weight machine is shown in Figure 4.14. During the test, the DT specimen sits on top of the anvil and is fractured by the striker tup of the drop-weight that is dropped directly above the DT specimen from an initial height, as shown in Figure 4.15. In the DRDC Atlantic tests, the mass of the drop-weight was 296 kg while the initial height of the drop was approximately 1 m. The dimensions of the DT specimen and the striker tup used in the DRDC Atlantic tests are shown in Figure 4.16 and Figure 4.17, respectively. The vertical velocity of the drop-weight was measured continuously during the drop. The DT fracture energy (E_{DT}) is then calculated as the difference between the initial potential energy (PE_i) and the final energy (PE_f) of the drop-weight after it travels a minimum vertical distance of 51 mm after contacting the specimen, as given by the following equation:

$$E_{DT} = PE_i - PE_f = \frac{1}{2}mv_i^2 + mg\Delta h - \frac{1}{2}mv_f^2 \qquad [4.6]$$

where, m is the mass of the drop-weight (296 kg), v_i is the velocity of the drop-weight just before contacting the specimen (4.33 m/s), g is the acceleration due to gravity (9.81 m/s^2), Δh is the minimum vertical distance the drop-weight travelled after contacting the specimen (51 mm) and v_f is the velocity of the drop-weight after travelling Δh.

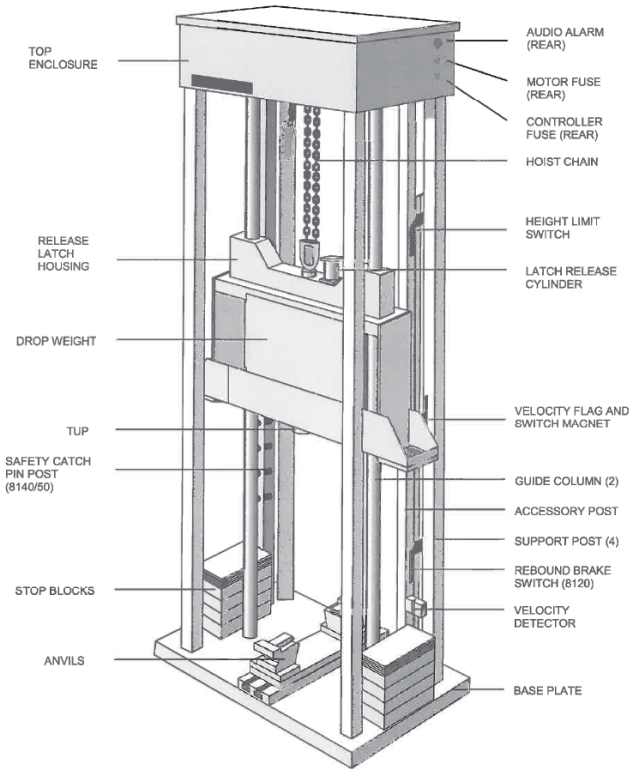

Figure 4.14: Series 8100 Drop-Weight Machine

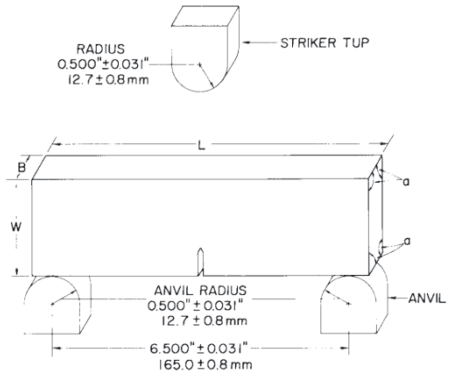

Figure 4.15: Dynamic Tear Specimen, Anvil Supports and Striker [10]

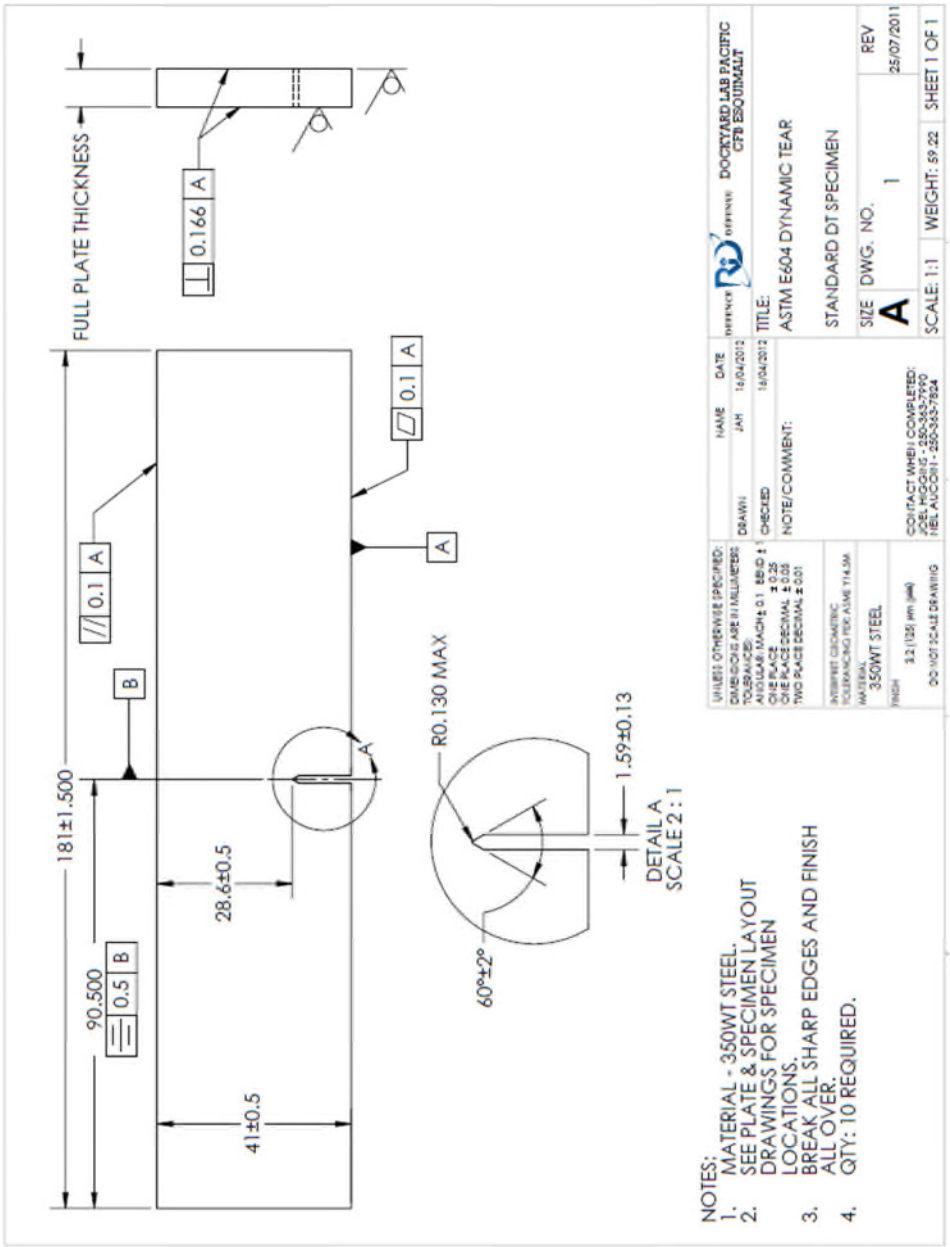

Figure 4.16: Dimensions of the Dynamic Tear Specimen

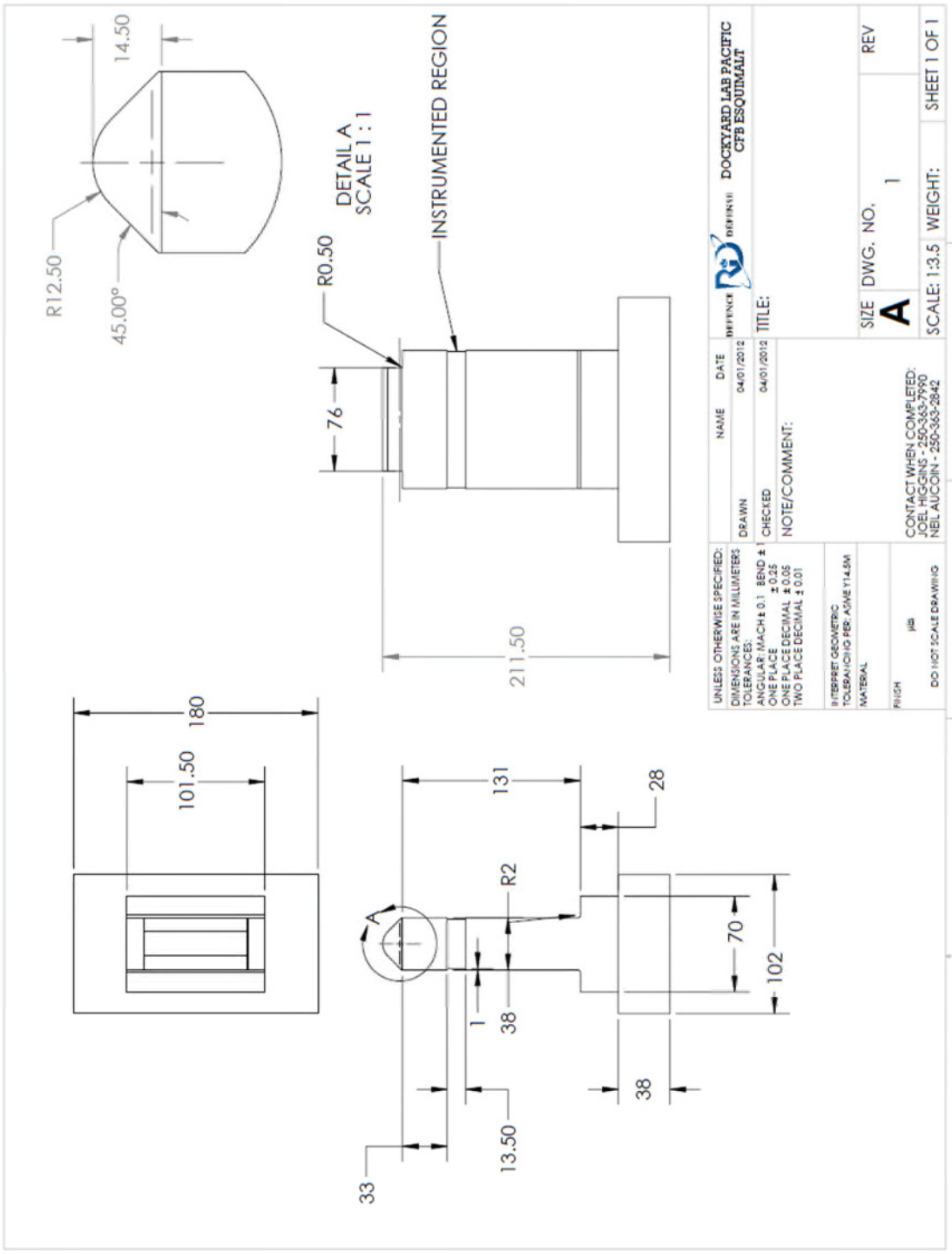

Figure 4.17: Dimensions of the Striker Tup for the Dynamic Tear Testing

4.2.2 Analysis Setup and Results

Figures 4.18 and 4.19 show side and overhead views, respectively, of the FE mesh used in the analyses. The center mesh resolution is 0.53 mm, and is graded out from the notch tip. Rollers are placed at the boundaries to simulate the knife edges. The tup is given an initial velocity of 4.34 m/sec, and the tup and specimen top are tied using contact surfaces.

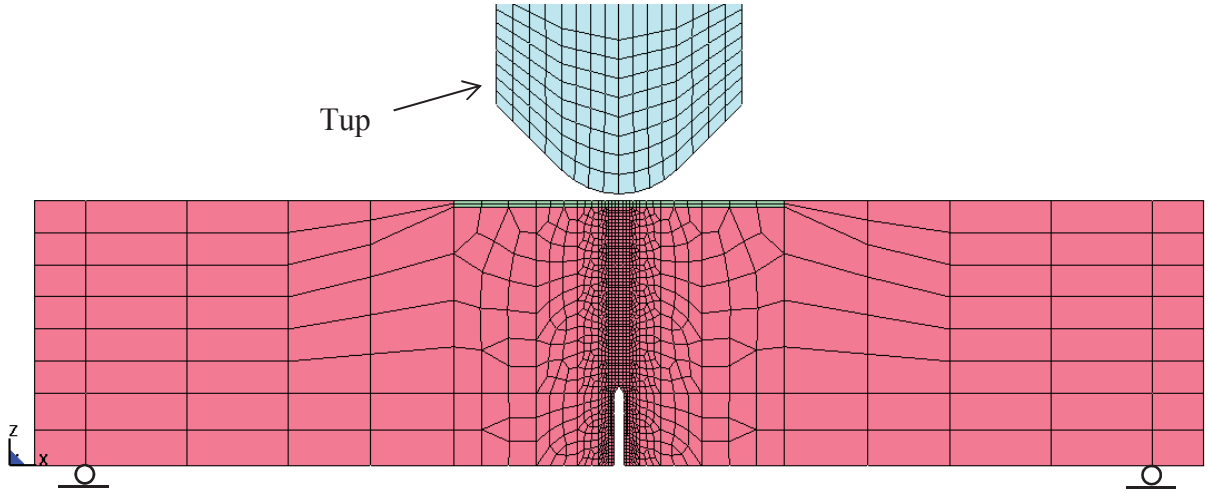

Figure 4.18: Drop Tower FE Mesh – Side View

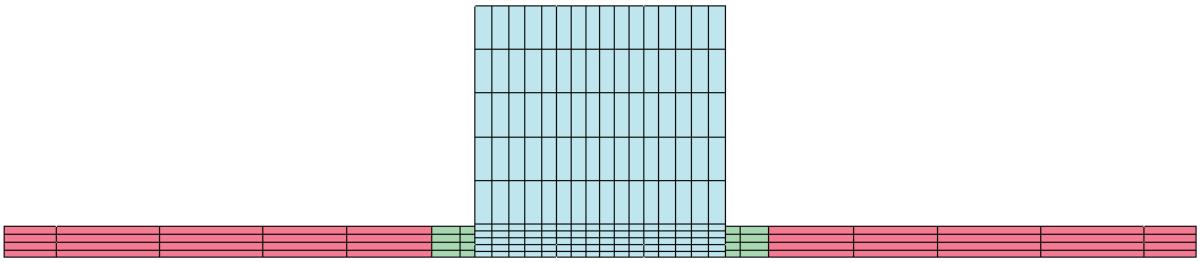

Figure 4.19: Drop Tower FE Mesh – Top View

The values of σ_{cr} and f_N were determined by using the procedure described in Section 4.0. Figure 4.20 shows f_N versus top shelf energy, assuming a ductile failure at 23° C. From comparison with the experimental energy, a value of 0.0331 was determined. Figure 4.21 shows σ_{cr} versus absorbed energy; from comparison with the 50% top shelf energy, a value of 1680 MPa was adopted.

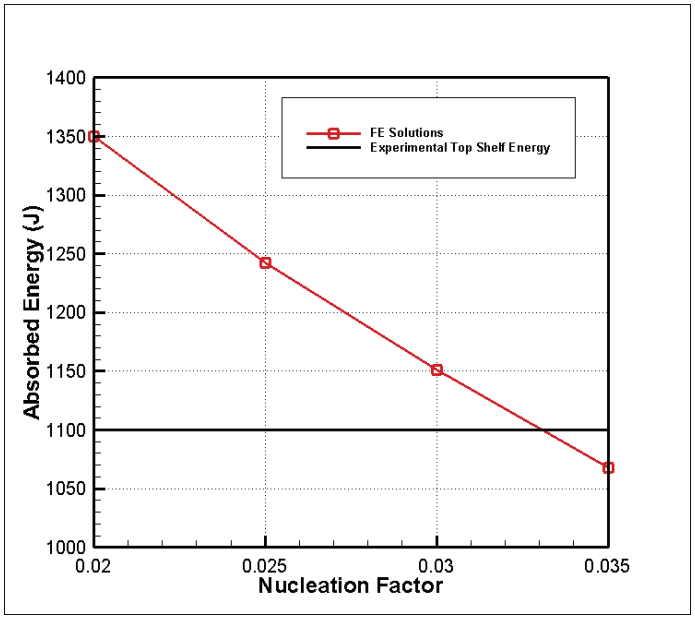

Figure 4.20: Determination of Nucleation Void Fraction

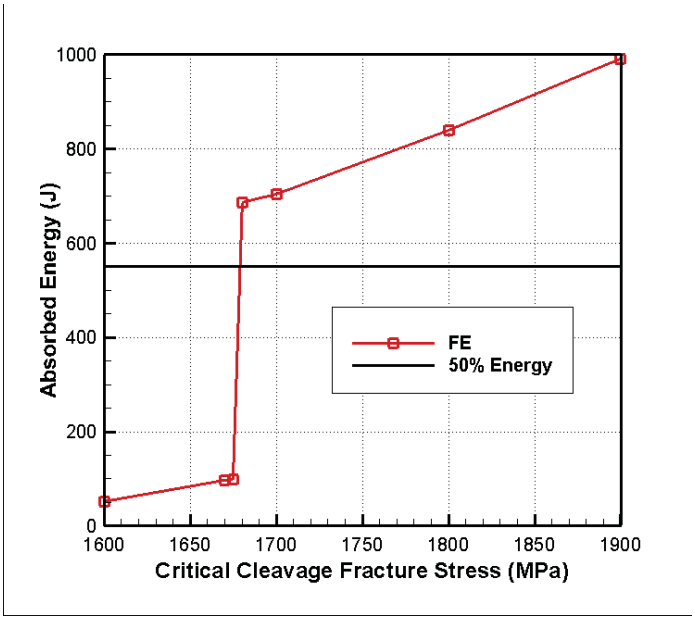

Figure 4.21: Determination of Critical Cleavage Fracture Stress

Figure 4.22 shows the DBT curve comparison. Although the transition temperatures are identical, the FE top shelf energy is significantly lower than the experimental results. Figure 4.23 and 4.24 show the deformed mesh just before and after failure. Before failure, approximately one-third of the elements fail in a ductile manner due to void nucleation. The remaining elements then rapidly fail in brittle fracture. This means that not all the elements are failing in a ductile manner; some are brittle fractures that absorb significantly less energy

than ductile failures. Hence the analysis absorbed energy is less than that of a fully ductile failure.

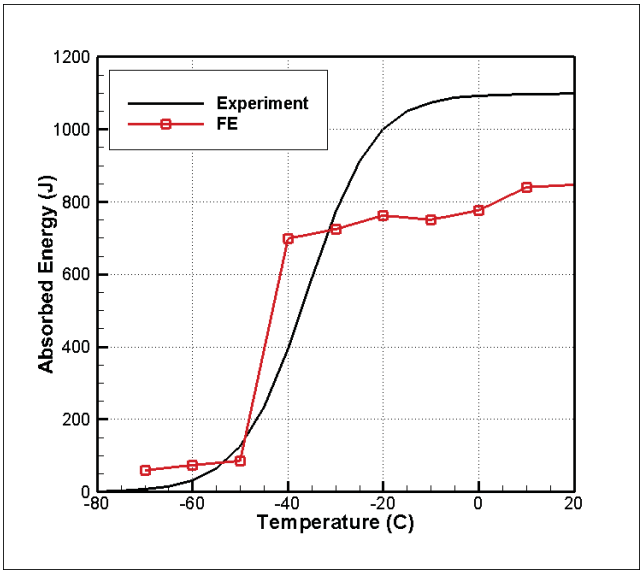

Figure 4.22: Drop Tower DBT Curve

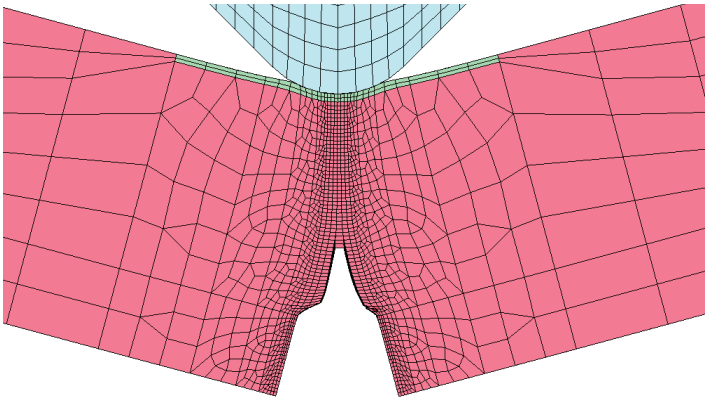

Figure 4.23: Drop Tower Just Before Failure

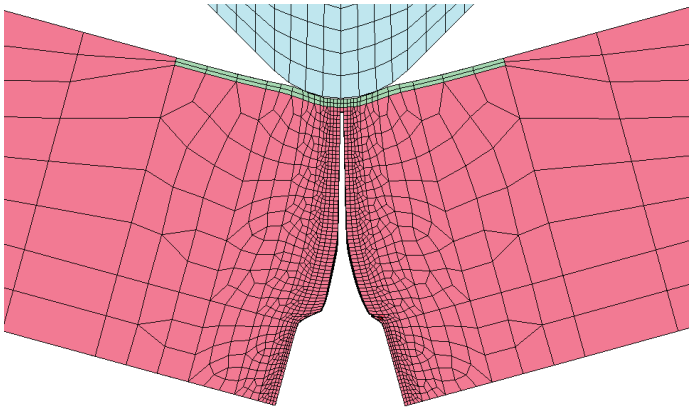

Figure 4.24: Drop Tower Just After Failure

Figure 4.25 shows a failed specimen at 20° C. From the wedge shape appearance, the failure appears to be that of a shear lip that extends most of the way through the specimen. The FE failure surface is not wedge shaped, and the ductile region is approximately 1/3 of the way through the specimen. The side view of the specimen in Figure 4.26 shows an angular ductile failure surface as opposed to the FE result, which shows a ductile failure surface that is approximately parallel to the initial crack. The FE brittle fracture surface is angular, but not ductile in nature.

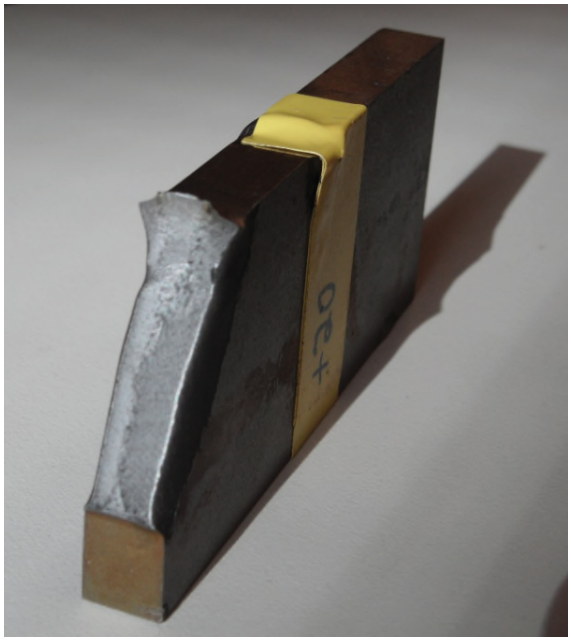

Figure 4.25: Drop Tower Specimen – Ductile Failure – View 1

Figure 4.26: Drop Tower Specimen – Ductile Failure – View 2

Upward adjustments were made to both f_N and σ_{cr} in an attempt to obtain a better fit for the top shelf energy. Although the top shelf energy was obtained, the ductile fracture consisted of only a few elements from the crack tip, and was considered invalid.

4.3 RESULTS DISCUSSION

The Charpy V-notch analyses yielded a good fit to the experimental DBT curve, and the correct failure surfaces were obtained. The drop tower tests yielded lower top shelf energies, and the experimental ductile failure surface was not obtained. Rather, ductile failure was obtained for approximately one-third of the fracture surface, followed by a sudden brittle failure that propagated through the remaining cross-section.

Calibration analysis results from the Charpy V-notch and drop tower tests yielded significantly different values for the nucleation void fraction, f_N, and the critical cleavage fracture stress, σ_{cr}, as shown in Table 4.2.

Table 4.2: Fracture Parameters From Tests

Parameter	Charpy V-Notch	Drop Tower
f_N	0.010	0.0331
σ_{cr} (MPa)	1950	1680

Since these parameters should yield unique values for a given material, there are possibly some factors that merit further investigation:

1) Lack of parameters – it is possible that more Gurson parameters must be considered in the parameter fit. Since there are a formidable number, a large study could be carried out just considering the two test series fit in this study. Because the project scope was rather extensive, a lack of resources precluded such an extensive fitting.
2) Nonlocal effects – σ_{cr} is specified as a point property, which may not be correct, since the fracture area may be more of a fracture process zone, and require an averaging of fracture quantities over a characteristic length.

Nevertheless, the analyses show qualitative results of both ductile and brittle fracture regimes, and these parameters will be used in the Charpy V-notch and explosive loading tests described in the next section. Since the plate is relatively thin for the explosive loading test, the drop tower parameters will be used for those simulations.

5.0 APPLICATIONS

5.1 CHARPY V-NOTCH PARAMETRIC STUDY

In this study, five different specimen widths were analysed to determine the effect of specimen width on the transition temperature. The mesh in Section 4.1.2 was used with specimen widths of 5.0, 7.5, 10.0, 12.5, and 15.0 mm. Figure 5.1 shows the absorbed energy vs. temperature of the 5 specimens compared with experiment. It can be seen that the top shelf energy increases with increasing specimen width, which is consistent with expected results. However, the expected result of an increase in transition temperature with increasing width is small at best; wider specimens tend more towards plane strain behaviour, and hence are expected to fail at a higher temperature. The 12.5 and 16.0 mm Charpys did not fail on the top shelf, and reached a maximum Charpy energy of 407 Joules.

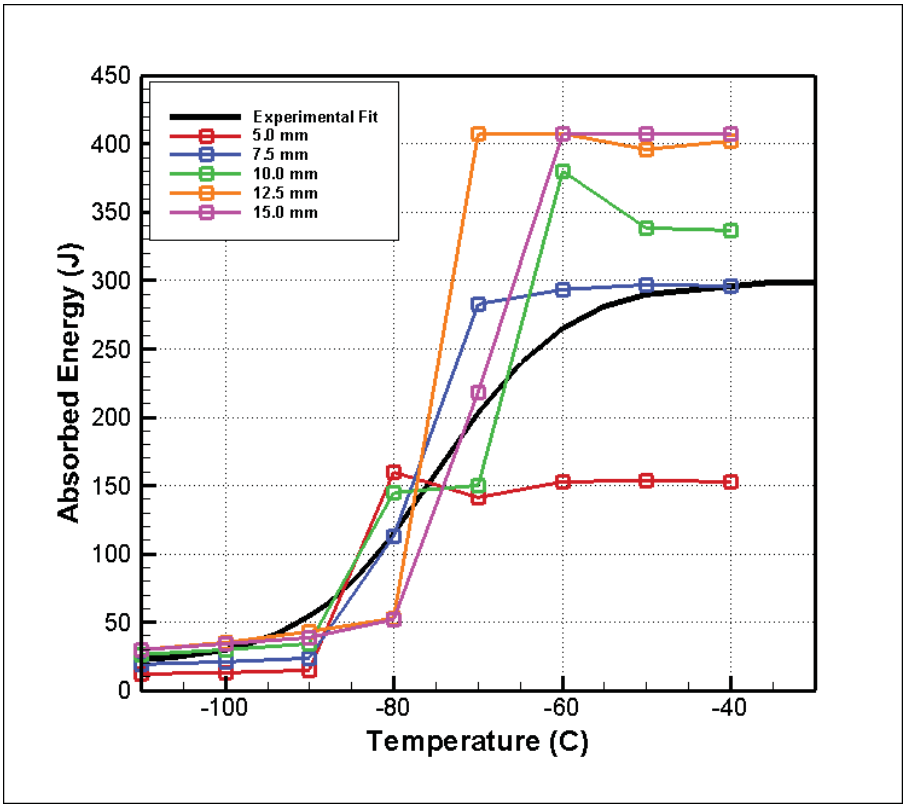

Figure 5.1: Effect of Specimen Width on Transition Temperature

5.2 EXPLOSIVE LOADING TEST

The explosive loading test is used to realistically simulate crack propagation in high strain rate military loading events. The explosive loading test consists of a rectangular steel plate which is cooled to a specified temperature and placed on a circular steel die. The steel plate has a crack starter weld placed at the plate center in order to start a propagating crack. An explosive

charge is placed above the plate and detonated. The crack failure surface is then examined to determine whether the failure is brittle or ductile. Figure 5.2 shows the test cross-section.

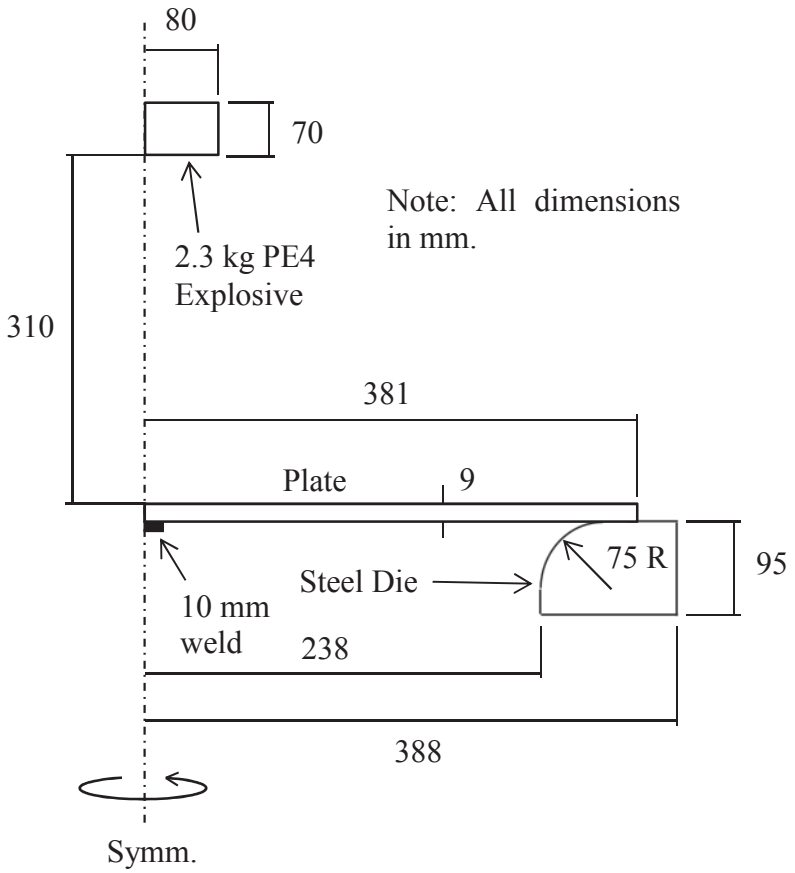

Figure 5.2: Explosive Loading Test Cross-Section

The explosive loading test is modelled in two separate phases. First, the loads are determined by performing a computational fluid dynamics (CFD) analysis. The loads are then placed on an LS-DYNA FE model to determine the plate fracturing characteristics.

Initially, it was thought that a blast load code such as Conwep [11] could be used as an approximation. However, preliminary analyses indicated that the load impulses were not sufficient to cause the plate to fracture. It was found that Conwep was inadequate in modelling explosive near-field effects, so Martec's explosive CFD code, Chinook [12], was used.

The grid used was axisymmetric, with a cell resolution of 2 mm square. The explosive C-4 was used, since PE-4 and C-4 are very similar in terms of explosive characteristics, and was detonated from the top down. Figures 5.3 and 5.4 are fringe plots of the explosive pressures before and after reflection; y is the symmetry axis, and the reflected surface is at y = 0. It can be seen that the charge cylindrical shape and close proximity have a major influence on the reflected pressures; the pressure shape and distribution are decidedly non-spherical.

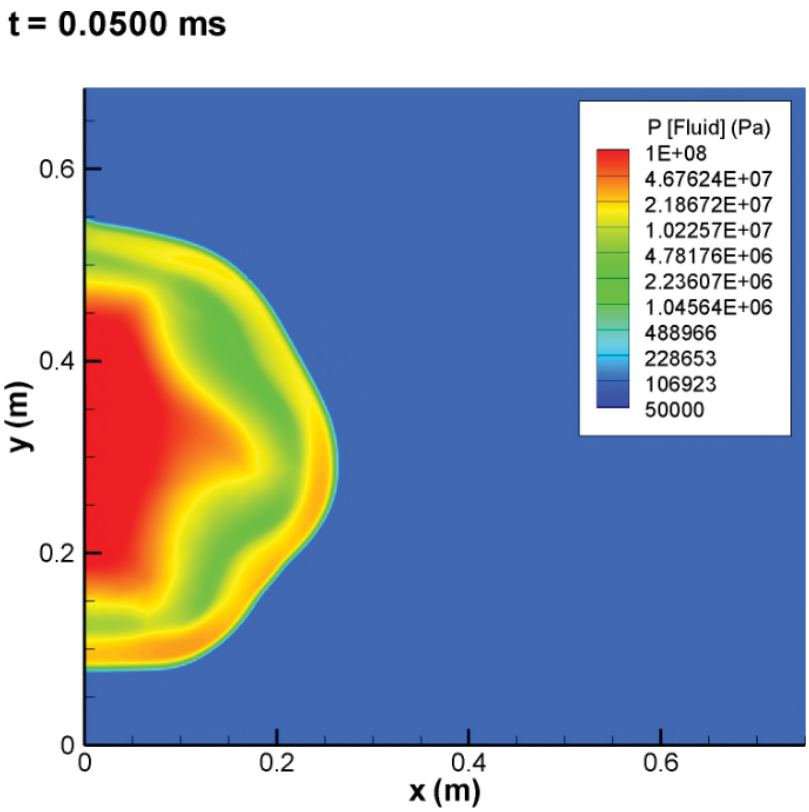

Figure 5.3: Explosive Pressures – t = 0.05 msec

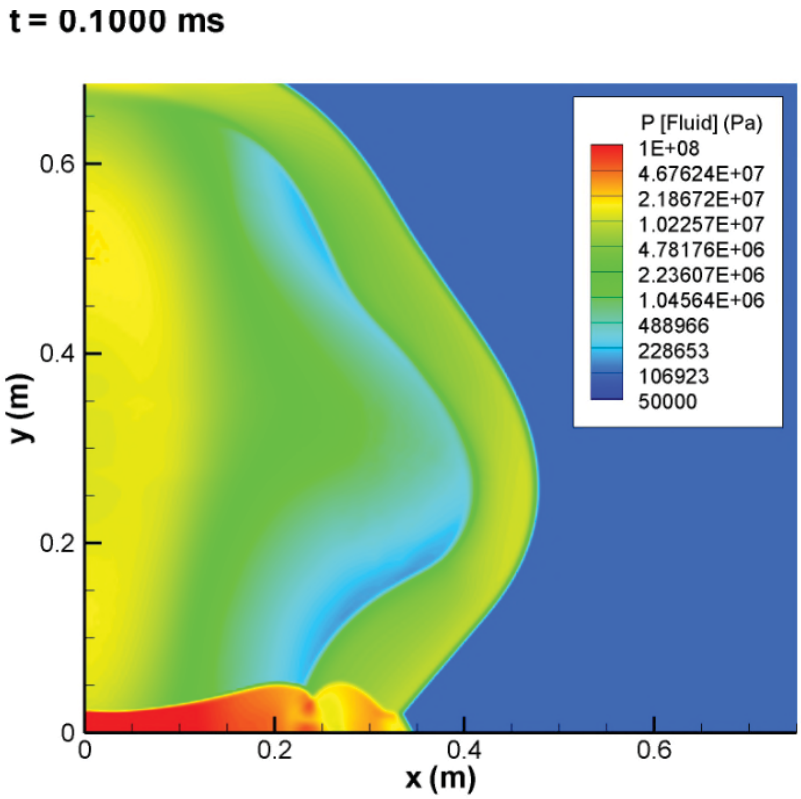

Figure 5.4: Explosive Pressures – t = 0.10 msec

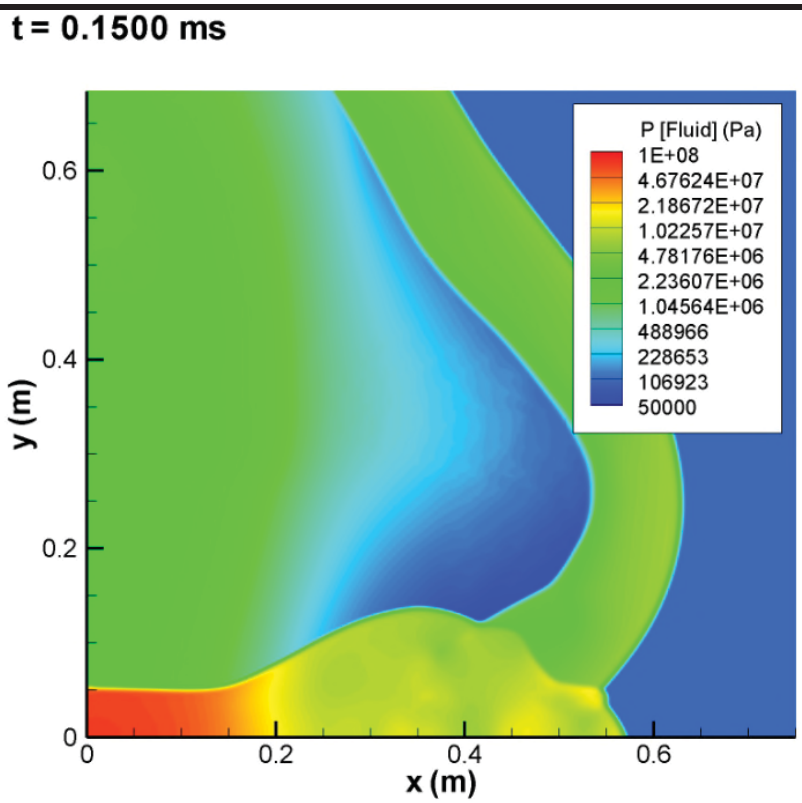

Figure 5.5: Explosive Pressures – t = 0.15 msec

Figures 5.6 and 5.7 are plots of spatial distributions of peak pressure and impulse, respectively, for both Conwep and Chinook simulations. It is seen that the CFD simulation predicts much larger peak pressures and positive phase impulses in the plate central region. Hence, accurate explosive physics modelling is crucial in obtaining correct loading behavior.

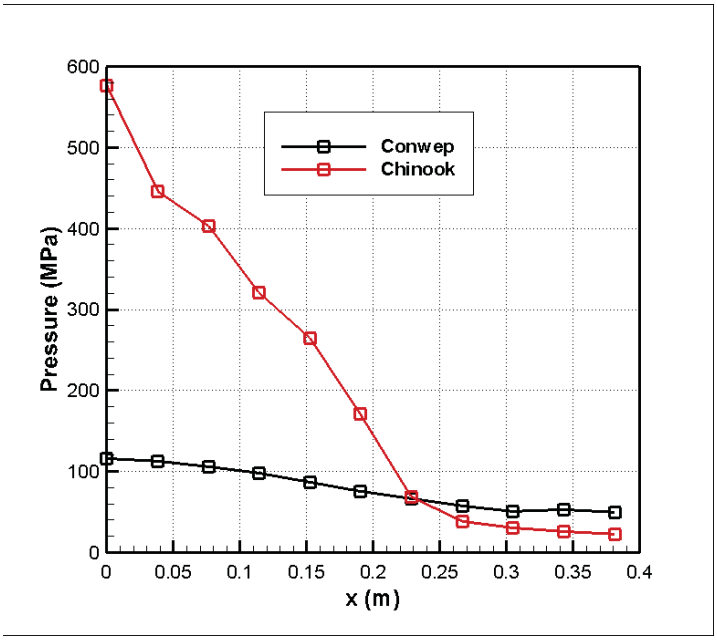

Figure 5.6: Peak Pressure Spatial Distribution

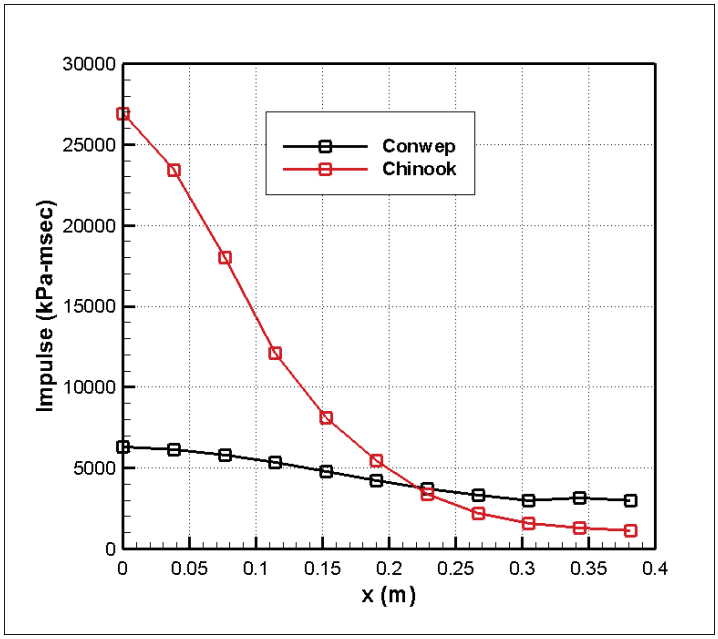

Figure 5.7: Impulse Spatial Distribution

Figure 5.8 and 5.9 show top and side views of the plate FE model. The plate is half-symmetric, and is modelled as round rather than square. The different colors on the top view denote different loading zones as specified in Figures 5.6 and 5.7. The loading is applied in the form of triangular pulses with the peak pressure being the apex. The impulse is used to determine the loading duration.

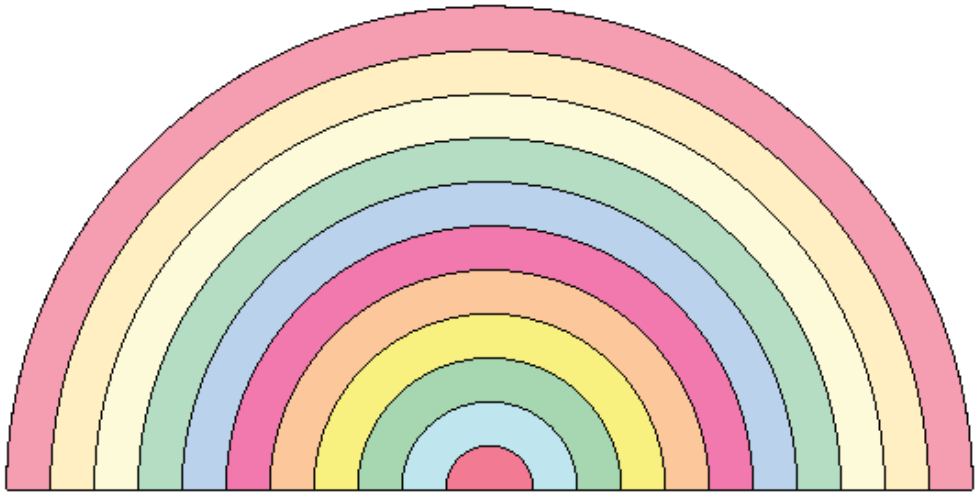

Figure 5.8: FE Plate Model - Top

The green curved region in Figure 5.9 is the die that the plate sits on. Contact surfaces are used to model the impact between the plate and die. The selected plate dimension was 9 mm.

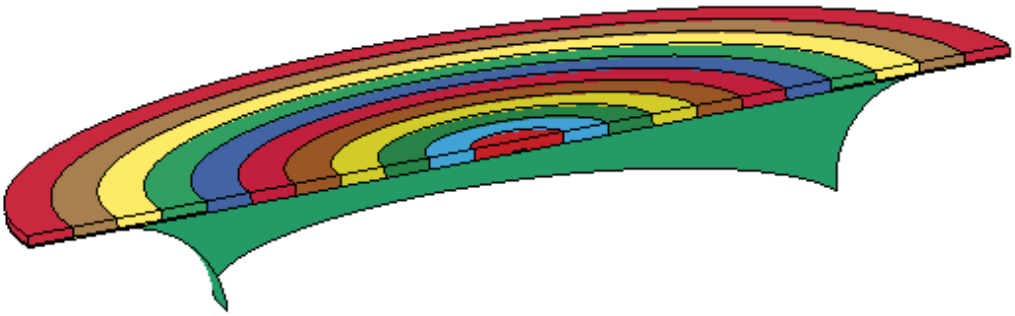

Figure 5.9: FE Plate Model – Side

Figure 5.10 shows the top mesh; the mesh is refined to 0.50 mm at the central region, and is graded out. Figure 5.11 shows the refined mesh at the plate central region; 6 through-thickness elements were used. Two crack types extending 10 mm over the central region were attempted; the first one was an edge crack in the first element, and the second was a through-thickness crack extending through the entire plate.

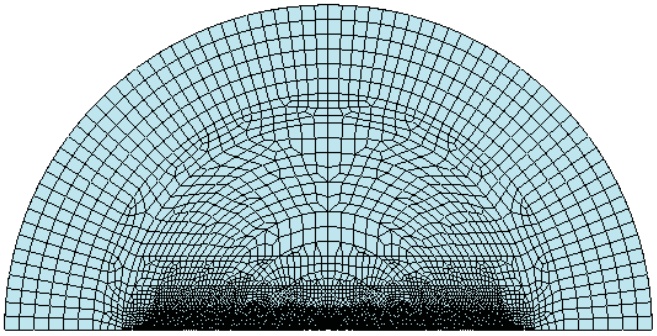

Figure 5.10: Plate Mesh – Full Top View

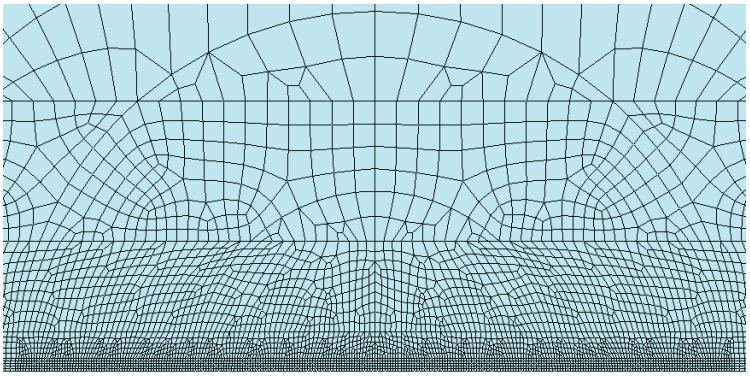

Figure 5.11: Plate Mesh – Central Region Top View

The edge crack was run at -50° C, and no crack propagation was found to occur. The through-thickness crack was then run, and the crack propagated to the plate edge. It was decided that the crack starter weld would provide a brittle heat affected zone (HAZ) in the crack vicinity, and that this would propagate through the thickness as well as radially. Hence, all runs were performed using the through thickness crack.

Figures 5.12-5.14 show the deformed shapes and fracture surfaces from top and side views for temperatures of -10°, 10°, and 23° C, respectively. The fracture surface on the side view is indicated with a darker color shade. The crack arrests for 10° and 23° C, and propagates nearly through the entire plate for -10° C. The failed surface at -10° C exhibits odd behavior at the crack ends; this is probably due to a large mesh gradation there.

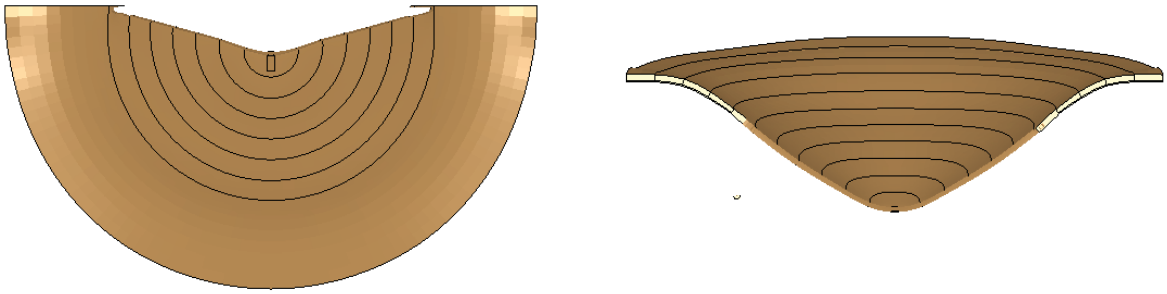

Figure 5.12: Deformed Shape at -10° C

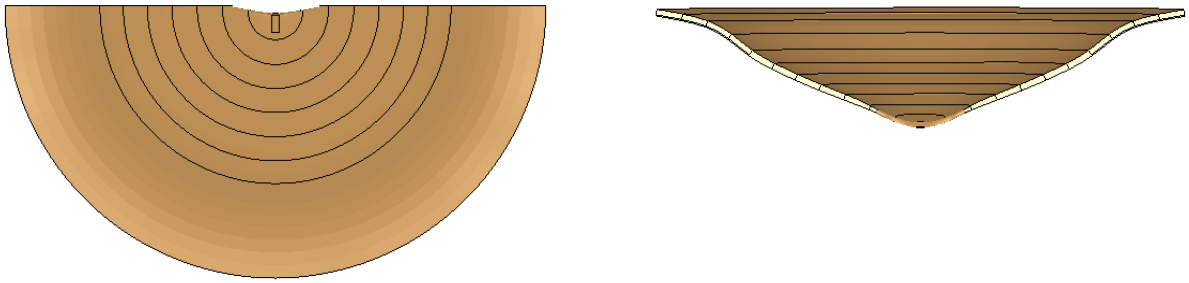

Figure 5.13: Deformed Shape at 10° C

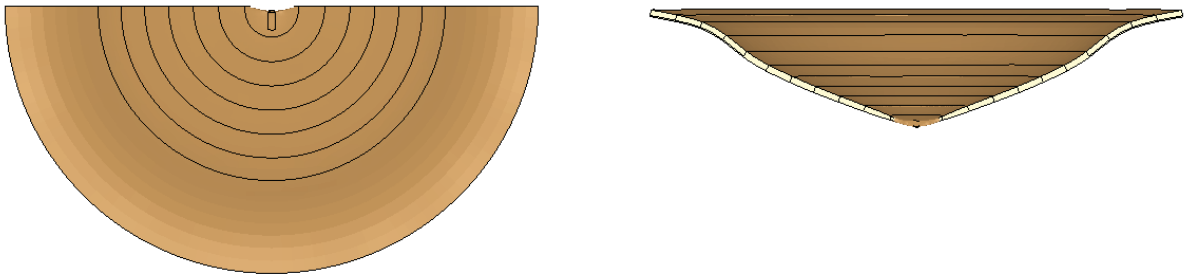

Figure 5.14: Deformed Shape at 23° C

From the analysis results, three basic failure modes were identified: brittle, ductile, and mixed mode. Figures 5.15-5.17 show the failure surfaces for each mode, and Table 5.1 describes the failure surface characteristics. The brittle mode occurred with no significant plastic straining i.e. no significant necking was observed. The ductile mode exhibited significant cross-section necking, and the mixed mode showed large deformations on the plate edges only. The mixed mode failure surface is indicative of shear lips forming on the plate top and bottom surfaces.

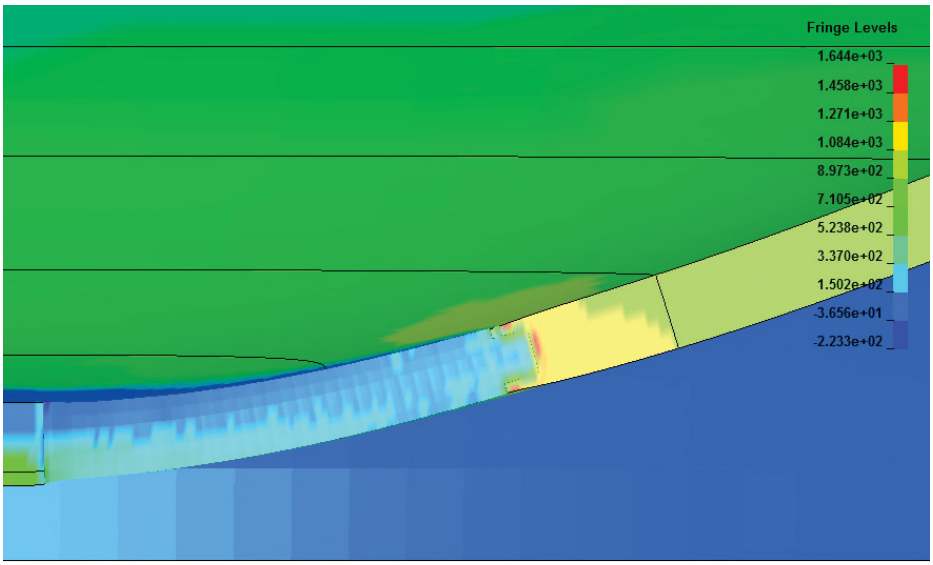

Figure 5.15: Brittle Fracture Surface (Maximum Principal Stress Plotted)

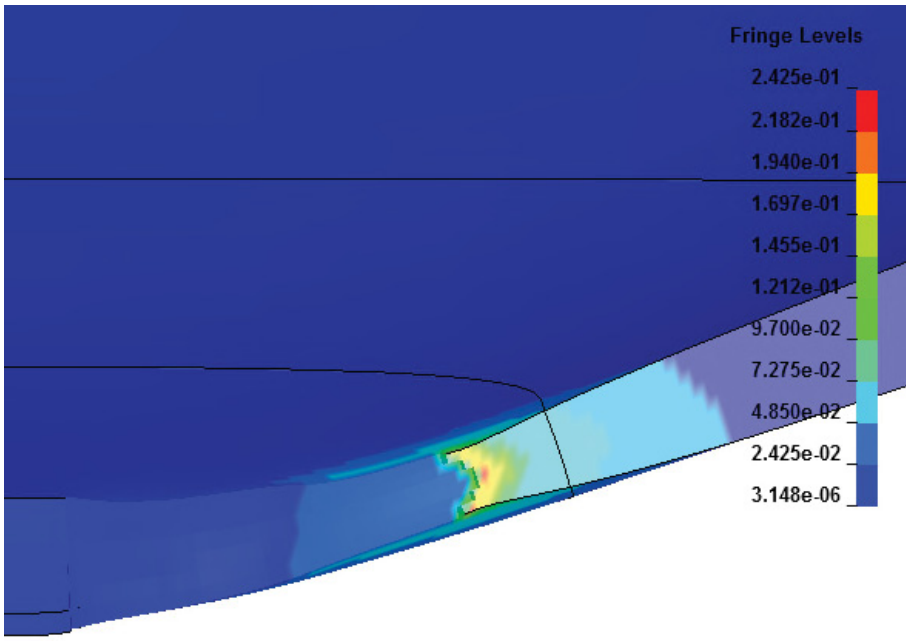

Figure 5.16: Ductile Fracture Surface (Void Fraction Plotted)

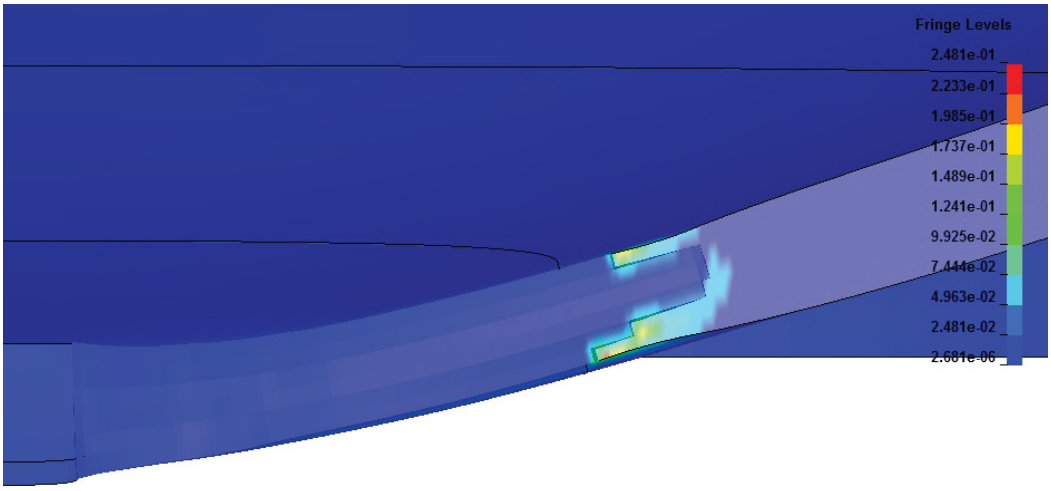

Figure 5.17: Mixed Mode Fracture (Void Fraction Plotted)

Table 5.1: Failure Mode Description

Failure Mode	σ_{cr} Exceeded	Void Fraction Exceeded
Brittle	All	None
Ductile	None	All
Mixed	Plate top and bottom	Plate center

The fibrosity is estimated by examining the failure surfaces of each run. The higher temperatures tend to fail in a 100% ductile manner, and lower temperatures fail with 0% fibrosity. However, there are temperatures where mixed fracture modes are present. To obtain these, the length of each ductile failure region is multiplied by the percentage of ductile cross-sectional elements. These lengths are summed and divided by the total crack length to compute the fibrosity. For example, the length of elements that fail according to Figure 5.17 would be multiplied by 1.0, and the failure length in Figure 5.17 would be multiplied by 0.333-0.5. This is a rough estimate and only gives an indication of the fibrosity magnitude.

Figures 5.18 and 5.19 show the fibrosity and plate energy absorbed versus temperature. Both fibrosity and plate energy show an approximate transition temperature around 0° to -10° C. It is noted here that the plate deflections were in the order of 135-180 mm, which is greater than the depth of the test setup (95 mm).

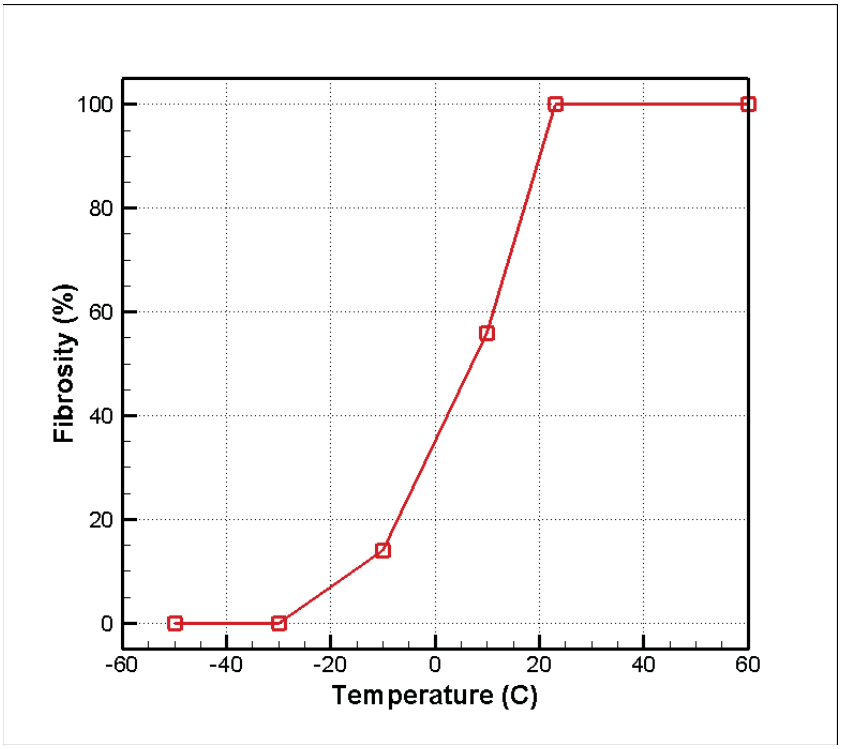

Figure 5.18: Fibrosity vs. Temperature

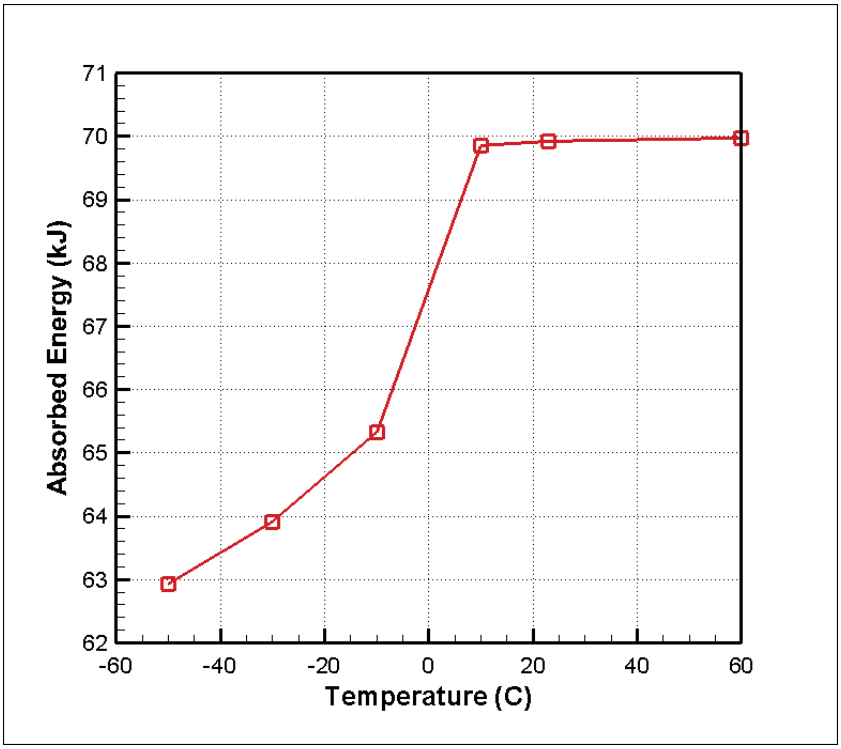

Figure 5.19: Plate Absorbed Energy vs. Temperature

6.0 CONCLUSIONS AND RECOMMENDATIONS

The fracture technology implemented in previous studies ([3], [8]) has been used here to model the ductile-to-brittle transition behavior of 3 different tests: Charpy V-notch, dynamic tear (drop tower), and explosive loading. The task results from Section 1 are summarized from the tasks given in Section 1 below.

6.1 TASK 1: MATERIAL PROPERTY CHARACTERIZATION

A curve fit was performed on flow stress vs. temperature data obtained from Bouchard [2]. The notched test data was examined, and it was determined that all failures were ductile; hence, Beremin parameters could not be computed for brittle fracture. However, the results were used in conjunction with the stress-strain curve fits to determine whether the static parameters were accurate. It was found that the ultimate load reached in all the tests were within 5% of experiment. As well, the area reductions at the minimum cross-section were computed, and it was determined that the FE area reduction predictions were consistently larger than experimental results. This was possibly due to neglecting void nucleation, growth, and coalescence, which would give larger cross-section expansions.

The 3 compact tension specimens were analysed, and computed J results were within 12% of the experimental values. Upon examination of the J calculation spreadsheets provided by the SA, it was found that small variations in the value of the precrack length resulted in large differences in J. The precrack effect was not included in the FE model; if the precrack effect is removed, the resulting values with and without precrack approximately bound the FE results.

6.2 TASK 2: DYNAMIC MODELLING

A literature search was performed regarding the flow stress dependency on strain rate. A publication was found [7] that contained data for HSLA 350 steel for strain rates up to 1000/sec. It was decided that this steel was similar enough in composition to 350WT steel to determine the strain rate dependency parameter, C, as 0.02.

Ductile and brittle parameters were then fit using available CVN and dynamic tear tests. Because the Gurson ductile model involves a multiparameter curve fit, it was decided that two fracture parameters would be varied; the void nucleation fraction, f_N, and the critical cleavage fracture stress, σ_{cr}. The value for f_N was determined from FE analysis of the experimental top shelf energy assuming a large σ_{cr}. The value for σ_{cr} was then determined using the transition temperature at 50% of the top shelf energy.

The Charpy analysis results yielded a good match to the experimental DBT curve, although the transitional area was more abrupt than the experiment. Comparison of the fractured area with photographs yielded good agreement. The dynamic tear results yielded a top shelf energy significantly lower than that of experiment. Examination of the failure surface determined that

the FE analysis exhibited ductile fracture for about one-third of the cross-section, followed by brittle fracture afterward. This was not the case for the experiment, which exhibited a wedge-like cup-cone failure for nearly the entire cross-section.

Comparison of f_N and σ_{cr} between the two tests revealed significant differences in values. This may have been due to a lack of fit parameters, or neglecting non-locality of the fracture process.

6.3 TASK 3: MODELLING THE SIZE DEPENDENCE OF FRACTURE

A parametric study was performed on CVN specimens to determine the effect of specimen width on the transition temperature. Specimens of five different widths were analysed using the fracture parameters determined for the CVN specimens in Task 2. It was determined that the top shelf energy increased with increasing width, but there was little or no difference in the transition temperature.

The explosive loading test setup of [13] was simulated in two stages. The first stage involved the determination of structural loading; two models were used, one using Conwep [11], and the other using Martec's flagship CFD blast code, Chinook. The models indicated significantly greater peak pressures and impulses from Chinook over Conwep. This indicates that explosive near-field effects play a large role in the accurate determination of explosive loads. Conwep is meant to be used as a far-field air blast application, and is not accurate for near-field problems. The second modelling stage was to apply the CFD loads onto the plate structure. The plate structure was modelled using 3-D solid elements with contact near the die areas. A through-thickness crack was used to simulate the effects of the crack starter weld. Fracture parameters from the dynamic tear test were used.

Analysis results indicated that there were ductile, brittle, and mixed mode fractures present at varying temperatures. Fibrosity and absorbed energy results indicated that the transition temperature was in the range of 0° to -10° C.

6.4 CONCLUSIONS AND RECOMMENDATIONS FOR FUTURE WORK

From examination of the FE results, the following is concluded:

1) The determination of flow stress as a function of temperature yielded good results for the simulation of the notched test and compact tension specimens. Failure loads for the notched tests were within 5% of experimental results, and the cross-sectional area measurements were reasonable. The calculated J values were close to the experimentally determined values.
2) The Charpy DBT test simulations yielded a good match to the experimental values. The FE ductile failure surfaces were similar to those from the experiment.
3) The dynamic tear DBT test simulations yielded significantly lower top shelf energy than the experiment. Examination of the ductile FE failure surface showed that the

failure mode was a combination of ductile and brittle fracture modes, in contrast to the fully ductile failure observed in the experiment.

4) The values for of f_N and σ_{cr} were markedly different between the CVN and dynamic tear tests.
5) The CVN parametric study yielded higher top shelf energies with increasing specimen thickness, which is consistent with expected results. However, the change in transition temperature with increasing thickness was relatively small at best. Since thicker specimens are closer to plane strain conditions, it was expected that the transition temperature would increase with increasing thickness.
6) The explosive loading test simulation yielded ductile failure modes for higher temperatures, and mixed and brittle modes for lower temperatures, which is consistent with expected results. In some cases, evidence of limited shear lip formation was found from the failures of the plate top and bottom surfaces.

The unexpected disparity between the CVN and dynamic tear tests needs to be resolved. Future areas of investigation may include:

1) Higher resolution models – because full 3-D models require excessive solution time, lower resolution models were used here. In order to capture details such as shear lip formation, finer resolution models may be required.
2) Nonlocal effects – a single stress value is used here for determination of brittle fracture. However, the stress field near a crack tip is singular, even for general elastic-plastic applications, and energy release rates such as J may have to be used in conjunction with σ_{cr}. This would make σ_{cr} a function of mesh size. A possible method is to compute the crack tip J for a uniform mesh, and determine the maximum principle stress at the failure J.
3) Ductile fracture parameter fits – more Gurson parameters may need to be considered for fitting. As well, these parameters may be functions of mesh size.

7.0 REFERENCES

(1) Bayley, C. (2013). Private Communication.

(2) Bouchard. R. (2004). A Study of the Fracture Process and Factors That Control Toughness Variability in Charpy V-Notch Specimens. PhD Thesis. University of Laval.

(3) Link, R.A., and Jiang, L. (2012). Development of a Micromechanical Failure Model. Martec Report TR-12-24.

(4) Beremin, F.N. (1983) A Local Criterion For Cleavage Fracture of a Nuclear Pressure Vessel Steel. Metallurgical Transactions A, Volume 14A, November, pp. 2277-2287.

(5) European Structural Integrity Society (1998). ESIS P6-98 – Procedure to Measure and Calculate Material Parameters For the Local Approach to Fracture Using Notched Tensile Specimens, ESIS, March.

(6) Bayley, C. (2013). Private Communication.

(7) Dietenberger, M., Buyuk, M., and Kan, S. (2005). Development of a High Strain Rate Dependent Vehicle Model. LS-DYNA Anwenderforum – Crash III.

(8) Link, R.A. (2013) Modelling of Specimen Fracture – Final Report. Martec Report TR 13-47.

(9) American Society for Testing and Materials (1996). ASTM E23-96 – Standard Test Methods for Notched Bar Impact Testing of Metallic Materials, ASTM.

(10) American Society for Testing and Materials (1983). ASTM E604-96 – Standard Test Method For Dynamic Tear Testing of Metallic Materials, ASTM.

(11) Hyde, D.W. (1988). Microcomputer Programs CONWEP and FUNPRO, Applications of TM5-855-1, "Fundamentals of Protective Design For Conventional Weapons" (Users Guide). Army Engineers Waterways Experiment Station, Vicksburg, MS Structures Lab.

(12) Martec Limited (2014). Chinook 2014 Manual, Software Manual SM-04-12. Martec Limited.

(13) Verdaasdonk, J.P., Spyker, R., and Sterjovski, Z. (2012). The Use of Modern High Strength Steel Grades in the Australian Air Warfare Destroyer (AWD). Proceedings, Pacific 2012 International Maritime Conference, Darling Harbour, Australia.

[14] Livermore Software Technology Corporation (2007). LS-DYNA Keyword Users Manual. LSTC.